ACS Catalysis

pubs.acs.org/acscatalysis Research Article

Elementary Steps, Site Requirements, and Support Effects in Methylcyclohexane Dehydrogenation Reactions on Dispersed Pd Nanoparticles

Zhongyao Zhang, Sai Chen, Trenton Otto, and Enrique Iglesia*

Cite This: ACS Catal. 2025, 15, 676–696 Read Online

ACCESS | Metrics & More | Article Recommendations | Supporting Information

ABSTRACT: Hydrogenation-dehydrogenation cycles enable the efficient storage, transport, and release of hydrogen via chemical means. Practical kinetic, thermodynamic, and H-density considerations make cyclic hydrocarbons the preferred organic hydrogen carriers. This study addresses the mechanism of methylcyclohexane (MCH) dehydrogenation to toluene (TOL), through methylcyclohexene (MCHE) intermediates on Pd nanoparticles (2−11 nm diameter) dispersed on Al_2O_3, SiO_2, MgO, and CeO_2. Turnovers occur on Pd surfaces densely covered with MCH-derived intermediates differing in isomeric structure and reactivity via sequential C−H activation elementary events, irrespective of nanoparticle size or support. The kinetically relevant step shifts from the second to the first H-abstraction step in MCH as temperature increases (from 453 to 553 K). The reactivity of Pd nanoparticle surfaces is insensitive to their size but supports with more competent Lewis acid−base (LAB) pairs lead to higher rates and stronger rate enhancements (relative to SiO_2) with decreasing temperatures, which reflect the lower coverages of less reactive intermediates when supports can scavenge desorbable species. These dense adlayers retain interstices within which dehydrogenation turnovers occur, but no longer expose the most distinctive low-coordination atoms prevalent on small nanoparticles, leading to the observed structure insensitivity of turnover rates. The prevalence of such adlayers leads to surfaces without the saturation hydrogen coverages expected for Pd surfaces devoid of such organic species. These mechanistic insights are consistent with (i) the elimination of support effect by titration of LAB pairs; (ii) initial rate transients that are inhibited by competent supports; (iii) the relative reactivity of metal-free supports for dehydrogenation of MCHE and methylcyclohexadienes (but not MCH); and (iv) measured kinetic effects of MCH, MCHE, and H_2 on turnover rates. The support effects provide strategies for maximizing the exposure of bare atom ensembles during dehydrogenation reactions. Its conceptual impact and practical significance are not restricted to the subject reaction in this study.

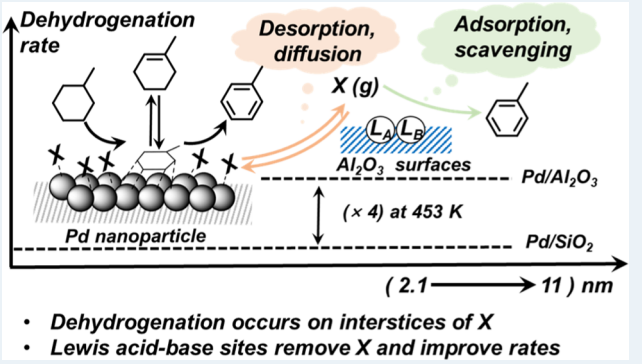

KEYWORDS: *cycloalkane dehydrogenation, C−H activation, nanoparticle size effect, nanoparticle-support synergy, palladium catalysts*

1. INTRODUCTION

The use of H_2 as an energy carrier requires its safe and efficient storage and handling. One strategy stores hydrogen atoms within organic molecules that can undergo selective hydrogenation-dehydrogenation reactions, thus allowing hydrogen to be stored at high volumetric and gravimetric densities and their transfer to markets in conventional vessels or their use to capture and store intermittent wind and solar energy.[1−3] Among these, cycloalkanes and polycyclic alkanes represent inexpensive and recyclable liquid organic carriers with significant hydrogen content (e.g., 7.1% wt, cyclohexane; 6.1% wt, methylcyclohexane; 7.3% wt, decalin).[1,4−6]

The recovery of H_2 from these alkanes via catalytic dehydrogenation requires the selective cleavage of C−H bonds (and the formation of H_2 and alkenes/arenes) in endothermic reactions that thermodynamically require modestly high temperatures (450−600 K) for practical single-pass yields.[7,8] Methylcyclohexane (MCH) is used here as an illustrative substrate because of its molecular simplicity, low freezing point (147 K), and moderate toxicity and cost.[9,10] MCH dehydrogenation forms H_2 and toluene (TOL) via a sequence of H-abstraction steps.[11,12] In spite of the apparent molecular simplicity of these dehydrogenation reactions, the intermediates and elementary steps involved and their kinetic relevance have remained the subject of enduring controversy, at least in part, because of the large number of plausible bound

Received: November 24, 2024
Accepted: December 11, 2024
Published: December 24, 2024

https://doi.org/10.1021/acscatal.4c07240
ACS Catal. 2025, 15, 676−696

intermediates and spectator species and their broad range of kinetic competence and surface coverages.[13−15]

Dispersed Pd nanoparticles dehydrogenate cycloalkanes by cleaving C−H bonds and recombining bound H atoms (H*) to form H_2,[16−18] but mechanism-based interpretations for kinetic trends are few and contradictory for cycloalkane dehydrogenation on Pd, in contrast with the more abundant, but similarly contradictory proposals for Pt and Ni catalysts.[19−21] Cyclohexane (CH) dehydrogenation rates on Pd/Al_2O_3 (at 448−483 K) were reported to be insensitive to CH pressure, leading to the proposal that surfaces were densely covered by CH-derived species, but without any insights about the kinetic relevance of any given C−H cleavage elementary step or bound intermediate and without any evidence for the effects of Pd nanoparticle size on surface reactivity.[22] Density functional theory suggested that the first C−H cleavage step in CH limited dehydrogenation rates on Pd(111) extended surfaces,[23] a conclusion that remains unconfirmed by experiments. There are no definitive studies (or even plausible heuristic inferences) about the nature and kinetic relevance of reactive and spectator bound species or about the consequences of Pd nanoparticle size or support identity for reactivity.

The contrasting reports of the consequences of support and metal nanoparticle diameter on cycloalkane dehydrogenation rates have been variously attributed to metal−support interactions that perturb nanoparticles electronically,[24] to unique electronic properties of low-coordinated Pt atoms at the edge sites that increase adsorption energies for alkanes,[25] or to product inhibition effects that depend on particle size.[26] MCH dehydrogenation turnover rates (at 663 K) were reported to decrease with increasing size on Pd nanoparticles (2−4 nm) dispersed on SiO_2 and Al_2O_3, but without detectable effects of the support identity on turnover rates.[27] In contrast, CH dehydrogenation turnover rates (at 543 K) were invariant with Pd nanoparticle size (2−5 nm) on carbon supports, leading the authors to classify such reactions as "structure-insensitive" without any mechanistic considerations about how the kinetically relevant cleavage of strong C−H bonds could be insensitive to the coordination of exposed metal atoms at nanoparticle surfaces.[28,29]

The absence of particle size effect on turnover rates has been reported for CO oxidation on Pt nanoparticles[30] and CO hydrogenation on Co nanoparticles,[31] because CO forms dense adlayers that obscure the structural features and intrinsic nonuniformity of metal nanoparticles. Similarly, dense adlayers of dehydrogenated species with different locations of double bonds, metal−carbon attachment points, and H-content are also ubiquitous during dehydrogenation and hydrogenolysis reactions on Ir, Rh, Pt, and Ru catalysts.[32,33] Other than hydrocarbon species, chemisorbed H atoms (H*) also form dense adlayers on Pt nanoparticles even at temperatures higher than those required for MCH dehydrogenation and modest H_2 pressures (10 kPa; at 473−673 K).[34] The effects of the dense adlayers consisting of unsaturated organic species lead to turnover rates that are insensitive to particle size, as confirmed here for MCH dehydrogenation on dispersed Pd nanoparticles.

This study reports kinetic trends and their mechanistic underpinnings for MCH dehydrogenation (at 453−553 K) on Pd nanoparticles dispersed on SiO_2, Al_2O_3, MgO, and CeO_2, as well as the effects of nanoparticle size on MCH dehydrogenation turnover rates. MCH dehydrogenation sequence involves the irreversible formation of methylcyclohexene (MCHE) isomers that are present at pseudo steady-state and subsequently converted to TOL. The effects of MCH and H_2 pressures on MCH dehydrogenation rates showed that the abstraction of the second H atom from MCH was the sole kinetically relevant step at 453 K; this kinetic relevance shifted to the first H-abstraction step with increasing temperature and became the sole limiting elementary step at 553 K. The effects of MCH and H_2 pressures on MCHE concentrations indicate that the abstraction of the second H atom from MCHE limited the rate of MCHE conversion to TOL at conditions that lead to MCH-MCHE equilibration at 453 K, which shifted to the first H-abstraction in MCHE at 553 K. These mechanistic conclusions are similar for Pd nanoparticles (2.1−11 nm) different in diameter and dispersed on SiO_2, Al_2O_3, MgO, and CeO_2 supports.

The identity of the support, however, influences MCH dehydrogenation rates at all conditions without any detectable differences in measured kinetic trends for Pd nanoparticles on different supports. Pd/Al_2O_3 catalysts showed higher MCH dehydrogenation turnover rates than Pd/SiO_2 (about 4-fold at 453 K); such support-induced rate enhancements increased as temperatures decrease (24-fold at 393 K), but the kinetic trends and their mechanistic underpinnings were not detectably influenced by the support identity. MCH dehydrogenation rates were insensitive to Pd nanoparticle size on a given support (SiO_2 or Al_2O_3), indicating that the observed rate differences do not reflect any effects of the support on the structure or electronic properties of Pd nanoparticles, because the more intimate contact between supports and smaller crystallites would lead to size-dependent turnover rates. Pd/SiO_2 mixed intimately with Al_2O_3 showed higher MCH dehydrogenation rates than Pd/SiO_2 (a factor of 1.5), suggesting that such rate enhancements do not require atomic contact between sites on Pd nanoparticles and on Al_2O_3, but benefit from the intimacy conferred by dispersing the nanoparticles on the more competent support.

The absence of particle size effect and the irrelevance of atomic contact between Pd nanoparticles suggest such rate enhancement should be attributed to an inhibitor-scavenging route. The inhibitor-scavenging route posits the accumulation of the less reactive species on Pd surfaces derived from MCH, which form TOL much more slowly than other more reactive intermediates but occupy Pd surfaces and compete with more reactive intermediates on the crowded surfaces that are ubiquitous during dehydrogenation catalysis. Such less reactive intermediates can desorb and get scavenged at Lewis acid−base (LAB) pairs on Al_2O_3 surfaces, thus decreasing their metal surface coverages and leading to an increased prevalence of more competent intermediates. The rate enhancements mediated by supports that expose LAB site pairs at surfaces and the underpinning phenomena that account for these effects have also been observed on Pt nanoparticles for its reverse reaction (toluene hydrogenation).[35] These effects of supports on rates of dehydrogenation[36,37] have previously invoked the concept of (reverse) hydrogen spillover,[38,39] shown to be implausible for supports that cannot form H^+-e^- pairs because of their insulating character.[40] Our work provides a strategy for using supports, as cocatalysts that enable the scavenging of less reactive species from nanoparticle surfaces, thus opening novel routes for the design of dehydrogenation catalysts.

2. METHODS AND MATERIALS

2.1. Catalyst Synthesis and Characterization. Pd nanoparticles were dispersed on SiO_2 (Davisil grade 62; 320 $m^2\ g^{-1}$ surface area; 1.15 $cm^3\ g^{-1}$ pore volume), Al_2O_3 (Sasol

https://doi.org/10.1021/acscatal.4c07240
ACS Catal. 2025, 15, 676−696

North American; 270 $m^2\ g^{-1}$ surface area; 0.57 $cm^3\ g^{-1}$ pore volume), MgO (Mallinckrodt; 98%; 0.25 $cm^3\ g^{-1}$ pore volume), and CeO_2 (Sigma-Aldrich; product number 544841) using incipient wetness impregnation methods and aqueous Pd-$(NO_3)_2$ solutions (Alfa Aesar; 8.5% wt $Pd(NO_3)_2$ in 15% wt HNO_3).[41,42] Supports were treated in flowing dry air (Praxair zero grade; 0.6 $cm_{air}^3\ g_{support}^{-1}\ s^{-1}$) at 973 K for 4 h and then heated in stagnant air at 373 K before impregnation with solutions of Pd precursors. Impregnated samples were treated in stagnant ambient air at 383 K for 8 h and then heated to 873 at 0.033 K s^{-1} and held for 3 h in flowing dry air (Praxair zero grade; 0.6 $cm_{air}^3\ g_{catalyst}^{-1}\ s^{-1}$), cooled to ambient temperature, heated to 773 K (at 0.033 K s^{-1}), and held for 2 h in flowing 50 kPa H_2 in He (Praxair UHP grade; 0.6 $cm_{gas}^3\ g_{catalyst}^{-1}\ s^{-1}$), and cooled down to ambient temperature; samples were then passivated by exposure to flowing 0.5 kPa O_2 (0.6 $cm_{gas}^3\ g_{catalyst}^{-1}\ s^{-1}$) in He for 2 h before exposure to ambient air. These samples are denoted as Pd/X-Y (X = SiO_2; Al_2O_3; MgO; and CeO_2), where Y indicates the mean nanoparticle diameter (eq 1) determined from transmission electron micrographs.

Transmission electron microscopy (TEM; Tecnai 12 microscope) was used to determine the distribution of Pd nanoparticle sizes in each passivated sample. Pd catalysts were ground into fine powders suspended in isopropanol and ultrasonicated for more than 1 h. A few drops of the suspension were placed onto holey carbon films mounted on 300 mesh copper grids (Ted Pella Inc.). Surface-averaged diameters for Pd particles ($\langle d\rangle_{TEM}$) were calculated from the number of particles (n_i) with a diameter of d_i using[43]

$$\langle d\rangle_{TEM} = \frac{\sum n_i d_i^3}{\sum n_i d_i^2} \tag{1}$$

by counting at least 300 particles for each sample.

Fractional Pd dispersions (D) were determined from volumetric uptakes of chemisorbed hydrogen on samples placed within a quartz U-tube and treated in flowing H_2 (1.33 $cm^3\ s^{-1}$; Praxair UHP grade) by heating from ambient temperature to 573 K at 0.083 K s^{-1}, holding for 1 h, evacuating in dynamic vacuum for 1 h at 573 K (TMU 071 P pump; Pfeiffer; rotary vane pump; Varian DS 302; 10^{-6} Pa), and then cooling to 373 K. H_2 uptakes were measured by dosing H_2 at a given pressure (Praxair UHP grade; 1−30 kPa) into a cell containing the treated samples at 373 K. The reported dispersion (D) values were estimated from H_2 uptakes (with a 1:1 surface stoichiometry for H and Pd-atoms) as a function of pressures after extrapolating them to zero pressure. The mean Pd nanoparticle diameter was calculated from these uptakes using

$$d_{Pd} = 6v_{Pd}/(Da_{Pd}) \tag{2}$$

where v_{Pd} is the atomic volume of a Pd-atom in its bulk crystalline metal form (14.7×10^{-3} nm^3) and a_{Pd} is the area of a Pd-atom at the surface of bulk metal crystallites (fcc lattice; 7.93×10^{-2} nm^{-2}).[44]

2.2. Measurements of Methylcyclohexane Conversion and Methylcyclohexene and Toluene Formation Rates.

Pd catalysts were used as aggregates (180−250 μm diameter) formed by pressing powders into pellets and crushing and sieving; they were loosely mixed with quartz granules (Sigma-Aldrich; 180−250 μm; treated in air at 973 K); such granules showed no detectable MCH reaction rates and were used to ensure the absence of bed temperature gradients imposed by endothermic dehydrogenation reactions and of any mass transfer corruptions of measured rates (details in Section S3, Supporting Information (SI)). Reaction rates were measured on aggregates placed within fritted quartz tubes and heated resistively using a three-zone furnace (Applied Test Systems); the target temperature of treatment or reaction was maintained by electronic controllers (Watlow) and measured with type K thermocouples (Omega) placed at the outer reactor wall and the axial bed midpoint.

Samples were treated in flowing 20% O_2/He (Praxair) by heating to 573 K at 0.083 K s^{-1} and holding for 1 h, in He (Praxair; 99.999%) for at least 0.25 h, and in 50 kPa H_2/He (Praxair UHP grade) at 573 K for 1 h. Samples were then brought to the target reaction temperature and He and H_2 inlet molar rates were set to maintain H_2 pressures (Parker mass flow controllers). MCH (Sigma-Aldrich; 99.9%) pressures were set by vaporization into H_2/He streams upon introduction as a liquid using a syringe pump (Parker Hamilton). All transfer lines between the liquid injection point and the gas chromatography (GC; Shimadzu 2014) were kept above 373 K to prevent condensation of reactants and products. Concentrations were measured by flame ionization after chromatographic separation in a capillary column (HP-1). MCH, TOL, and 1MCHE were fully resolved and identified from the retention times of chemical standards. In most instances, the concentrations of 4-methylcyclohexene (4MCHE) and 3-methylcyclohexene (3MCHE) could not be accurately measured because of their trace amounts and/or elution times that overlapped with those for the MCH reactants. Methylcyclohexadiene (MCHD) isomers, even if formed at concentrations in equilibrium with MCH-H_2 reactants (e.g., ~10^{-17} Pa MCHD for 1 kPa MCH; 4 kPa H_2; 453 K), would remain well below chromatographic detection limits.

MCH conversion rates (and MCHE and TOL formation rates) were measured on all Pd-containing catalysts and Pd-free SiO_2 and Al_2O_3. MCH conversion rates were also measured on intimate mixtures of Pd/SiO_2 with Al_2O_3 (1:10 mass ratios) prepared by grinding them in a mortar and pestle, pressing the resulting powders into a wafer, and then crushing and sieving to retain aggregates (180−250 μm diameter). TOL and MCHE concentrations in the effluent stream were measured at different MCH (0.1−24 kPa) and H_2 (1−24 kPa) pressures and temperatures (453−553 K). Two chromatographic protocols were used in these experiments. Protocol A required cryogenic cooling and allowed analysis every 0.5 h and was able to isolate MCHE intermediates. Protocol B (~0.13 h) was used to capture the initial approach to steady-state rates, but it could not isolate MCHE peaks or measure their concentrations.

Measured MCH conversion rates ($r_{measured}$) to TOL were corrected for approach to equilibrium (η_{TOL}) to determine the forward reaction rates (r_f)

$$r_f = r_{measured}/(1 - \eta_{TOL}) \tag{3}$$

$$\eta_{TOL} = \frac{[TOL][H_2]^3}{K_{TOL}[MCH]} \tag{4}$$

Here, [MCH], [TOL], and [H_2] represent the MCH, TOL, and H_2 pressures (in units of bars); K_{TOL} is the equilibrium constant for TOL and H_2 formation from MCH (from tabulated enthalpy and entropy data[45]). All forward rates (r_f, after the initial approach to steady-state rates) reported here were also corrected for any intervening changes in rates caused by deactivation or activation, assumed to reflect the covering (or

https://doi.org/10.1021/acscatal.4c07240
ACS Catal. 2025, 15, 676−696

Table 1. Support Identity, Pd Content, Dispersion, and Mean Nanoparticle Diameters from TEM and H_2 Chemisorption for Pd-Based Catalysts

catalyst	support	Pd content (% wt)	mean Pd nanoparticle diameter (nm, TEM[a])	mean Pd nanoparticle diameter (nm, H_2 chemisorption[b])	Pd dispersion[c]
Pd/SiO_2-5.7	SiO_2	0.2	5.7(±0.6)	6.8	0.15
Pd/SiO_2-11	SiO_2	1.2	11(±1.1)	15	0.07
Pd/Al_2O_3-2.1	Al_2O_3	0.2	2.1(±0.3)	2.7	0.37
Pd/Al_2O_3-6.3	Al_2O_3	1.2	6.3(±1.0)	9.3	0.11
Pd/MgO-6.7	MgO	0.2	6.7(±0.6)	7.9	0.13
Pd/CeO_2-8.4	CeO_2	0.2	8.4(±1.4)	---	---

[a]Surface averaged diameter of Pd nanoparticles from TEM calculated with eq 1, Section 2.1. All micrographs can be found in Figure S2, SI. [b]Mean Pd nanoparticle diameter from H_2 chemisorption calculated by eq 2, Section 2.1. [c]Estimated via H_2 chemisorption, Section 2.1. Pd/CeO_2 chemisorption measurements are not accurate because the partial reduction of CeO_2 leads to significant hydrogen coverages on support surfaces.

uncovering) of the Pd nanoparticle surfaces by less reactive (or unreactive) organic species. Increasing H_2 pressure during MCH dehydrogenation led to higher reaction rates over time, as less reactive species were hydrogenated, thus uncovering some Pd sites and establishing a new steady-state. The correction procedure involved comparing rates at the end and start of each condition period to estimate and account for fractional changes in the number of accessible sites. This change was used to correct all rates to the steady-state at time zero for MCH conversion rates on Pd surfaces covered by less reactive species. Details of these procedures are included in Section S1.2, SI.

2.3. Reaction of Methylcyclohexene and Methylcyclohexadiene on Oxide Supports. Reactions of MCHE isomers (1MCHE; 3MCHE; and 4MCHE) (Sigma-Aldrich; 99%) and 1,4-MCHD (Sigma-Aldrich; 99%) were also measured on metal-free SiO_2 and Al_2O_3 samples to determine any potential additive contributions to measured rates, as well as the reactivity of these supports as potential scavengers of less reactive species that can cover Pd surfaces. MCHE and MCHD reactions (453−513 K) were measured by diluting reactants with *n*-octane (Sigma-Aldrich; anhydrous, 99%) to achieve pressures (4−64 Pa) that resemble those prevalent MCHE intermediates during steady-state MCH dehydrogenation (MCHD intermediates were not detected). *n*-Octane did not react on metal-free oxide supports at the temperature of these experiments (453−513 K). Metal-free supports used in these experiments were ground into fine powders, pressed into wafers, and crushed and sieved into aggregates (180−250 μm diameter). The treatment procedures, equipment, and chromatographic protocols were the same as those described in Section 2.2.

2.4. Titration of Lewis Acid−Base Pairs by Propionic Acid during MCH Dehydrogenation. Carboxylic acids titrate Lewis acid−base (LAB) pairs on Al_2O_3 surfaces[46] and have been used to titrate TiO_2 and ZrO_2 surfaces and to measure the number of LAB pairs active in aldol condensation and ketonization reactions.[46−49] Propionic acid was used here to titrate LAB pairs on Al_2O_3 and to probe their role in mediating the observed rate enhancements conferred by Al_2O_3 supports onto Pd nanoparticles. Similar experiments previously showed that the TOL hydrogenation rate enhancements conferred by Al_2O_3 on Pt nanoparticles were suppressed by propionic acid.[35] Propionic acid (PA, Sigma-Aldrich, 99.5%) was mixed with liquid MCH reactants and used to replace MCH reactants on Pd/Al_2O_3 (453 K; 4 kPa H_2; 1 kPa MCH) after rates reached steady values; rates were then measured upon contact of samples with PA-MCH mixtures and after removal of PA from the inlet stream. These experiments were carried out using the equipment and analysis protocols used to measure MCH dehydrogenation kinetic trends (Section 2.2).

3. RESULTS AND DISCUSSION

3.1. Dispersion of Pd Nanoparticles on Different Supports. Table 1 shows the Pd content, mean nanoparticle diameter (from TEM and chemisorption methods), and fractional Pd dispersion, together with the notation used for each sample. TEM gave mean diameters of Pd nanoparticles on Al_2O_3 supports of 2.1 and 6.3 nm for the 0.2 and 1.2% wt Pd samples. The mean Pd nanoparticle diameters on SiO_2 supports were 5.7 and 11 nm for the samples with 0.2 and 1.2% wt Pd. The mean diameters of Pd nanoparticles on MgO and CeO_2 were 6.7 and 8.4 nm (0.2% wt Pd in each sample). Hydrogen adsorption isotherms are shown in Figure S1 (Supporting Information; SI) on these samples and their fractional Pd dispersions are listed in Table 1. Mean nanoparticle diameters calculated from H_2 uptakes (eq 2) are in good agreement with those determined from micrographs (eq 1).

3.2. Effects of Methylcyclohexane, Methylcyclohexene, and H_2 Pressures on Methylcyclohexane Dehydrogenation Rates and Implications for the Kinetic Relevance of Elementary Steps and Intermediates. Scheme 1 depicts a sequential reaction network that includes the detected (or anticipated) gaseous intermediates in MCH conversion to TOL. TOL was the predominant product formed (>99% selectivity) with 1-methylcyclohexene (1MCHE) as the only other detectable product that could be accurately isolated at all conditions; 4-methylcyclohexene (4MCHE) was detected

Scheme 1. Reaction Sequence for the Formation of Gaseous Intermediate Species during MCH Dehydrogenation Reactions[a]

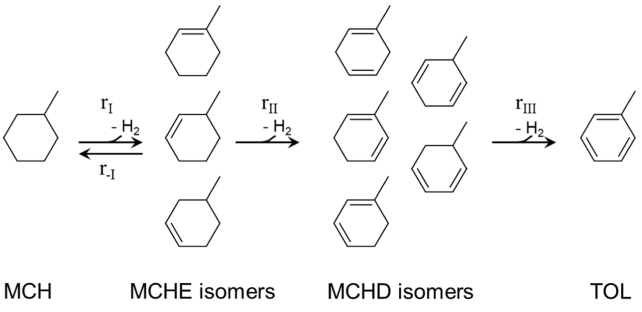

[a]r_I and r_{-I} represent forward and reverse rates for MCH conversion to MCHE; r_{II} represents the forward rate of MCHE conversion to MCHD and r_{III} for MCHD conversion rate to TOL.

https://doi.org/10.1021/acscatal.4c07240
ACS Catal. 2025, 15, 676−696

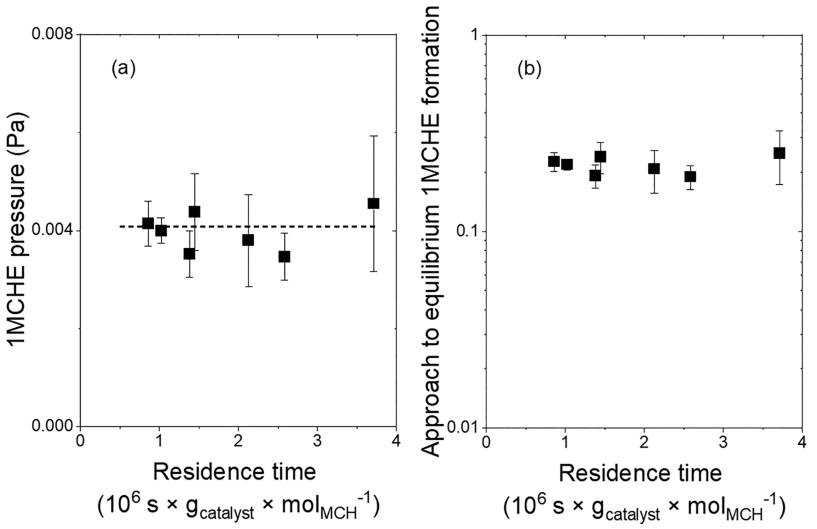

Figure 1. (a) 1MCHE pressure versus residence time for MCH dehydrogenation and (b) approach to equilibrium for 1MCHE formation on Pd/Al_2O_3-2.1 at 1 kPa MCH; 4 kPa H_2; 453 K. The dashed line indicates the trend.

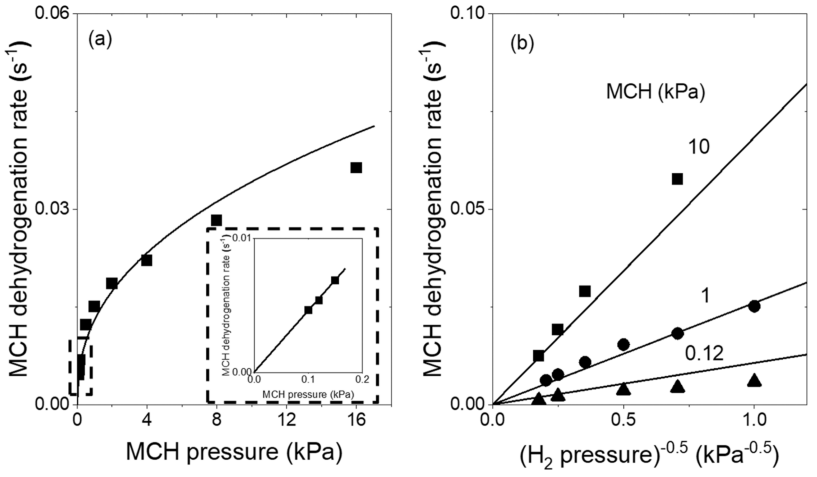

Figure 2. MCH dehydrogenation rates (r_I, Scheme 1) on Pd/Al_2O_3-2.1 at 453 K at different (a) MCH pressures (and 4 kPa H_2) and (b) (H_2 pressure)$^{-0.5}$ values (and 10 kPa (■); 1 kPa (●) and 0.12 kPa (▲) MCH). The inset in Figure 2a shows the enlargement at low MCH pressure (0−0.2 kPa). Solid curves and lines represent the regression of all rate data to the functional form of eq 7.

and quantified only with much longer chromatographic protocols, which showed that the MCHE isomers were in equilibrium with each other. MCHD concentrations, even if present in equilibrium with the prevalent MCH and H_2 pressures, would be below detection limits at the conditions of these experiments (e.g., 10^{-17} Pa at 1 kPa MCH, 4 kPa H_2, 453 K).

The intermediate formation of gaseous MCHE isomers allows independent assessments of the reversibility and kinetic relevance of the sequential reactions that form MCHE and convert them to TOL. The data in Figure 1a show that 1MCHE pressures are unaffected by changes in bed residence time (through changes in MCH inlet molar rates or catalyst amount) or by changes in conversion caused by deactivation, consistent with the presence of MCHE at pseudo steady-state concentrations. The approach to equilibrium for MCH conversion to MCHE (step I, Scheme 1) is given by

$$\eta_I = \frac{[\text{MCHE}][H_2]}{K_{\text{MCHE}}[\text{MCH}]} \quad (5)$$

Here, [MCH], [MCHE], and [H_2] are the respective pressures (in units of bar) and K_{MCHE} is the equilibrium constant for MCHE formation from MCH (from reported enthalpies and entropies for MCHE formation[45,50]). The data in Figure 1b show that η_I values for 1MCHE formation are much smaller than unity at all residence times (1 kPa MCH; 4 kPa H_2; 453 K), suggesting that step (I) in Scheme 1 is essentially irreversible, a conclusion that remains valid at all pressures and temperatures used in this study (453−553 K; 0.5−4 kPa MCH; 1−16 kPa H_2; Figure S8, SI). The irreversible nature of MCHE formation, the constant MCHE pressures at different conversions and residence times, and the formation of TOL as the predominant product (>99% selectivity) indicate that:

(i) MCHE intermediates are present at pseudo steady-state levels and MCHE formation rates are essentially equal to the MCHE conversion rates to TOL.

(ii) MCH dehydrogenation rates (the sum of net formation rates of MCHE and TOL) are essentially the same as TOL formation rates.

https://doi.org/10.1021/acscatal.4c07240
ACS Catal. 2025, 15, 676−696

MCH dehydrogenation rates (r_{MCH}) and TOL formation rate (r_{TOL}) can therefore be related to the rates of step I (r_I) and step II (r_{II}) by

$$r_{MCH} = r_{TOL} = r_I(1 - \eta_I) = r_{II} \quad (6)$$

The kinetic relevance of the elementary steps of the first stage (step I; Scheme 1) determines the kinetic trends of MCH dehydrogenation rates with MCH and H_2 pressures, because the reversibility of H-abstraction steps and recombinative H* desorption would affect the dependence of MCH dehydrogenation rates on H_2 pressure. The data in Figure 2a show that MCH dehydrogenation rates on Pd/Al_2O_3-2.1 increase linearly at first (below 0.15 kPa) and then sublinearly with MCH pressure. MCH dehydrogenation rates decrease with increasing H_2 pressure at each MCH pressure (at 0.12, 1, and 10 kPa MCH; 453 K; 1−32 kPa H_2; Figure 2b) in a manner accurately captured by an inverse dependence on $\sqrt{[H_2]}$

$$r_I = k_{MCH}\frac{[MCH]}{\sqrt{[H_2]}}\theta_*^{\gamma_{TS}} \quad (7)$$

Here, [MCH] and [H_2] denote their respective pressures, γ_{TS} is the number of contiguous unoccupied Pd surface atoms required to bind the transition state (TS) that mediates the kinetically relevant step for MCH dehydrogenation to MCHE, θ_* is the fraction of the Pd surface atoms that remain bare during reaction, and k_{MCH} is the lumped rate and thermodynamic parameters reflected in an apparent rate constant. The solid lines and curves in Figure 2 represent the regression of all rate data to the functional form of eq 7, for the case of θ_* as a single-valued function of MCH pressure, but independent of H_2 pressure. Such agreement between measured trends and model predictions indicates that θ_* depends on MCH pressure but not on H_2 pressure. All regressed parameters are shown in Section 3.6 after a full derivation of the kinetic model based on elementary steps is described.

Equation 7 and the data in Figures 2a,b show that θ_* depends on MCH pressure as a result of detectable coverages of MCH-derived species, but not on H_2 pressure, consistent with coverages of such species that are kinetically detectable but insensitive to H_2 pressures. The linear increase in MCH dehydrogenation rate (or MCHE formation rate) at low MCH pressures (below 0.15 kPa) suggests that Pd surfaces are sparsely covered with the reactive intermediates at these low pressures; the onset of curvature at higher pressures reflects an increase in the coverage of MCH-derived species and a concomitant decrease in θ_* (Figure 2a), but without any effects of H_2 on such coverages (Figure 2b). The functional form of eq 7 suggests that the kinetically relevant TS for MCH dehydrogenation to MCHE (step I, Scheme 1) contains a MCH molecule from which a single H-atom has been removed. Therefore, the first H-abstraction step of MCH must be quasi-equilibrated, and MCH dehydrogenation rates, which are **limited** by the formation of MCHE in step I (Scheme 1), are **limited** by the second H-abstraction step from MCH reactants.

MCHE concentrations are set by the rates of its formation (r_I; Scheme 1) and consumption (r_{II}; Scheme 1), which become essentially equal at pseudo steady-state (eq 6). The rate equation for MCHE consumption, expressed in terms of MCHE and H_2 pressures, can be inferred from measured MCHE pressures and used to provide independent evidence for the identity and reversibility of the elementary steps for step II in Scheme 1. This second stage does not limit MCH dehydrogenation or TOL formation rates at the conditions of this work, but it would become the sole rate-limiting step at conditions that lead to MCH-MCHE equilibration (step I; Scheme 1). The data in Figure 3 indicate that 1MCHE/MCH ratios are independent of

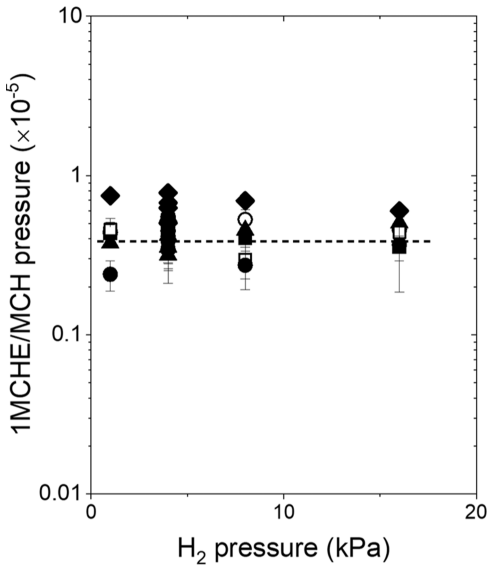

Figure 3. 1MCHE/MCH pressure ratio at 453 K on Pd/Al_2O_3-2.1 (■), Pd/Al_2O_3-6.3 (□), Pd/SiO_2-5.7 (●), Pd/SiO_2-11 (○), Pd/MgO-6.7 (▲) and Pd/CeO_2-8.4 (◆) for 0.5−4 kPa MCH and 1−16 kPa H_2 as a function of H_2 pressure. The dashed line indicates the trend.

MCH and H_2 pressures (at 453 K), an observation confirmed for all Pd catalysts. These trends require, in turn, that r_I and r_{II}:

(i) depend similarly on H_2 pressure;
(ii) involve bare atom ensembles similar in size for the binding of their respective kinetically relevant TS;
(iii) contain numerator terms that are proportional to MCH and MCHE pressures, respectively.

Therefore, the rate equation for MCHE conversion to TOL (r_{II}) can be deduced from eq 7 to be

$$r_{II} = k_{MCHE}\frac{[MCHE]}{\sqrt{[H_2]}}\theta_*^{\gamma_{TS}'} \quad (8)$$

where γ_{TS}' is the number of contiguous bare Pd surface atoms required to bind the transition state (TS) that mediates the kinetically relevant step for the conversion of MCHE to TOL (step II; Scheme 1), and k_{MCHE} is the lumped rate and thermodynamic parameters reflected in the apparent rate constant. When η_I is much smaller than unity (Figures 1b and S8), eqs 6−8 can be combined to give

$$\frac{[MCHE]}{[MCH]} = \frac{k_{MCH}}{k_{MCHE}}\theta_*^{\gamma_{TS}-\gamma_{TS}'} \quad (9)$$

The data in Figure 2 show that θ_* depends on MCH pressure, but not on H_2 pressure. The data shown in Figure 3 indicate, in turn, that the right side of eq 9 is independent of MCH, MCHE, or H_2 pressures; consequently, the ensembles required to bind the TS for the steps that limit MCHE formation (step I; Scheme 1) and conversion (step II; Scheme 1) are similar in size ($\gamma_{TS}' = \gamma_{TS}$). The MCHE and H_2 pressure terms in eq 8 show that the TS for the kinetically relevant step in MCHE conversion (step II; Scheme 1) has the molecular composition of a MCHE molecule from which one H-atom has been removed and therefore, the

https://doi.org/10.1021/acscatal.4c07240
ACS Catal. 2025, 15, 676−696

Scheme 2. Sequence of Elementary Steps for MCH Reactions on Pd Surfaces[a]

$$\boldsymbol{TH_6(g)} + (\gamma_6\,*) \overset{K_1}{\rightleftharpoons} TH_6(\gamma_6{}^*) \quad (1)$$

$$TH_6(\gamma_6{}^*) + (\gamma_5 - \gamma_6 + 1)\,* \overset{K_2}{\rightleftharpoons} TH_5(\gamma_5{}^*) + H^* \quad (2)$$

$$TH_5(\gamma_5{}^*) + (\gamma_4 - \gamma_5 + 1)\,* \xrightarrow{k_3} TH_4(\gamma_4{}^*) + H^* \quad (3)$$

$$TH_4(\gamma_4{}^*) \overset{K_3'}{\rightleftharpoons} \boldsymbol{TH_4(g)} + \gamma_4\,* \quad (3')$$

$$TH_4(\gamma_4{}^*) + (\gamma_3 - \gamma_4 + 1)\,* \overset{K_4}{\rightleftharpoons} TH_3(\gamma_3{}^*) + H^* \quad (4)$$

$$TH_3(\gamma_3{}^*) + (\gamma_2 - \gamma_3 + 1)\,* \xrightarrow{k_5} TH_2(\gamma_2{}^*) + H^* \quad (5)$$

$$TH_2(\gamma_2{}^*) \overset{K_5'}{\rightleftharpoons} \boldsymbol{TH_2(g)} + \gamma_2\,* \quad (5')$$

$$TH_2(\gamma_2{}^*) + (\gamma_1 - \gamma_2 + 1)\,* \overset{K_6}{\rightleftharpoons} TH_1(\gamma_1{}^*) + H^* \quad (6)$$

$$TH_1(\gamma_1{}^*) + (\gamma_0 - \gamma_1 + 1)\,* \overset{K_7}{\rightleftharpoons} TH_0(\gamma_0{}^*) + H^* \quad (7)$$

$$TH_0(\gamma_0{}^*) \overset{K_8}{\rightleftharpoons} \boldsymbol{TH_0(g)} + \gamma_0\,* \quad (8)$$

$$2H^* \overset{K_9}{\rightleftharpoons} \boldsymbol{H_2(g)} + 2\,* \quad (9)$$

[a] $TH_n(\gamma_n{}^*)$ denotes species with n H-atoms added to TOL (TH_0) and includes all locations of the H-atoms and C−Pd bonds. Unidirectional arrows denote irreversible steps, bidirectional arrows indicate reversible steps. $TH_n(g)$ represents the gaseous species of TH_n.

second H-abstraction from MCHE would become the kinetically relevant step at conditions that enable MCH-MCHE equilibration (step I; Scheme 1). The kinetic relevance of the elementary steps in step III (MCHD conversion to TOL; Scheme 1) cannot be elucidated from measured rates because MCHD gas phase concentrations are present well below detection limits.

Scheme 2 shows a sequence of elementary steps and bound species for the conversion of MCH to TOL and for the formation and desorption of MCHE and MCHD. A multisite adsorption model (details in Section S2.2, SI)[43] is required to describe coverages of intermediates, because different intermediates along the reaction coordinate may require binding ensembles that differ in size. For instance, $TH_n(\gamma_n{}^*)$ (n is an integer from 0 to 6; Scheme 2) represents all positional isomers (H and Pd−C locations) of a bound intermediate that has n more H-atoms than TOL (TH_0) and is bound at an ensemble of γ_n contiguous Pd surface atoms. For MCH molecules bound on Pd surfaces ($TH_6(\gamma_6{}^*)$) and in equilibrium with MCH(g), this multisite adsorption model gives a coverage

$$\theta_{TH_6(\gamma_6^*)} = \gamma_6 K_{TH_6}[TH_6]\theta_*{}^{\gamma_6} \quad (10)$$

where $[TH_6]$ is the contacting pressure of MCH in the fluid phase, γ_6 is the number of contiguous Pd surface atoms required to bind MCH, θ_* is the fractional coverage of unoccupied sites, $\theta_{TH_6(\gamma_6{}^*)}$ is the fractional coverage of $TH_6(\gamma_6{}^*)$, and K_{TH_6} is the adsorption constant for MCH molecules at ensembles consisting of γ_6 contiguous Pd surface atoms.

The data in Figure 2 (at 453 K) indicate that the kinetically relevant transition state for MCH dehydrogenation to MCHE has the molecular composition of a TH_5 moiety bound at a γ_5-atom ensemble. This requires, in turn, that the removal of the second H atom from MCH be the sole kinetically relevant step (step 3; Scheme 2). Step 1 (MCH adsorption), step 2 (the first H-abstraction of MCH), and step 9 (recombinative H* desorption) are in quasi-equilibrium during steady-state MCH dehydrogenation reactions

$$\theta_{TH_6(\gamma_6^*)} = K_1[TH_6]\theta_*{}^{\gamma_6} \quad (11)$$

$$\theta_{TH_5(\gamma_5^*)}\theta_{H^*} = K_2\theta_{TH_6(\gamma_6^*)}\theta_*{}^{\gamma_5-\gamma_6+1} \quad (12)$$

$$K_9\theta_{H^*}{}^2 = [H_2]\theta_*{}^2 \quad (13)$$

The rate of step 3 is then

$$r_3 = k_3\theta_{TH_5(\gamma_5^*)}\theta_*{}^{\gamma_4-\gamma_5+1} \quad (14)$$

Equations 11−14 can be combined to give

$$r_3 = \alpha'\frac{[MCH]}{\sqrt{[H_2]}}\theta_*{}^{\gamma_4+1}\ (\alpha' = \gamma_6 k_3 K_2 K_1\sqrt{K_9}) \quad (15)$$

where k_n and k_{-n} represent forward and reverse kinetic parameters for the nth elementary step and K_n represents the equilibrium constant for the nth elementary step in Scheme 2. MCH dehydrogenation rates are described by eq 7 (from measured kinetic trends in Figure 2) and eq 15 (derivation from the kinetic model above); thus, the k_{MCH} and γ_{TS} terms correspond to $\gamma_6 k_3 K_2 K_1\sqrt{K_9}$ and $\gamma_4 + 1$, respectively. Section S2.1 shows the derivation procedures and the identity of the most abundant surface intermediates (MASI) that depend on MCH pressures and affect the value of θ_*. The coverage of the MASI must be independent of H_2 pressure to satisfy the functional form of eq 15.

For MCHE conversion to TOL (step II; Scheme 1), step 3′ (MCHE adsorption/desorption), step 4 (the first H-abstraction of MCHE), and step 9 (recombinative H* desorption) are in quasi-equilibrium during steady-state MCH dehydrogenation reactions. Step 5 (the second H-abstraction of MCHE) must then be the kinetically relevant step

$$r_5 = \alpha''\frac{[MCHE]}{\sqrt{[H_2]}}\theta_*{}^{\gamma_2+1}\ (\alpha'' = \gamma_4 k_5 K_4 K_3'\sqrt{K_9}) \quad (16)$$

Measured MCHE formation rates (Figure 2) and MCHE pressure (Figure 3) are accurately described by eqs 8 and 16; thus, the k_{MCHE} and γ'_{TS} terms (eq 8) correspond to $\gamma_4 k_5 K_4 K_3'\sqrt{K_9}$ and $\gamma_2 + 1$ (eq 16), respectively. In the next section, these mechanism-derived rate equations will be

https://doi.org/10.1021/acscatal.4c07240
ACS Catal. 2025, 15, 676−696

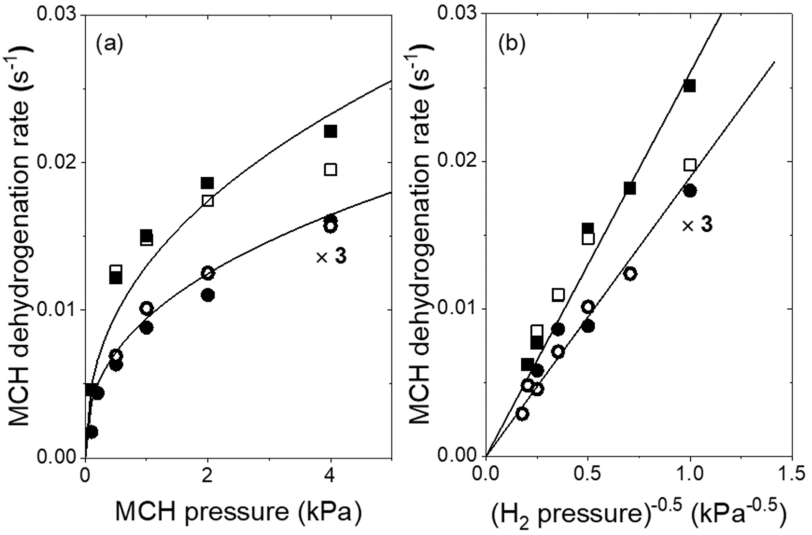

Figure 4. MCH dehydrogenation rates as a function of (a) MCH pressure (4 kPa H_2 at 453 K) and (b) (H_2 pressure)$^{-0.5}$ (1 kPa MCH at 453 K) on Pd/Al_2O_3-2.1 (■), Pd/Al_2O_3-6.3 (□), Pd/SiO_2-5.7 (●) and Pd/SiO_2-11 (○). Data on the silica-supported catalysts have been magnified by a factor of 3. Solid curves and lines represent the regression of rate data to the functional form of eq 7.

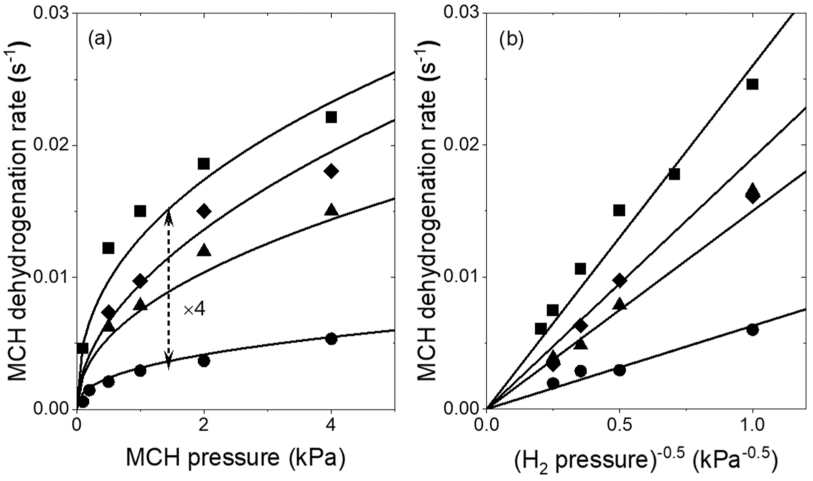

Figure 5. MCH dehydrogenation rates as a function of (a) MCH pressure (4 kPa H_2 at 453 K) and (b) (H_2 pressure)$^{-0.5}$ (1 kPa MCH at 453 K) on Pd/Al_2O_3-2.1 (■), Pd/SiO_2-5.7 (●), Pd/MgO-6.7 (▲), Pd/CeO_2-8.4 (◆). Solid curves and lines represent the regression of rate data to the functional form of eq 7.

investigated for Pd nanoparticles of different diameters (2.1−11 nm) dispersed on different supports, which might affect the identity or kinetic relevance of the elementary steps and intermediates involved in these reactions.

3.3. Effects of Pd Nanoparticle Diameter and Support on Rates of Methylcyclohexane Dehydrogenation. The effects of MCH and H_2 pressures on MCH dehydrogenation rates (r_1) are shown in Figure 4 for Pd/Al_2O_3 catalysts with mean nanoparticle diameters of 2.1 nm (used in Section 3.2) and 6.3 nm and for Pd/SiO_2 catalysts with 5.7 and 11 nm mean diameters. The data in Figure 4 show that MCH dehydrogenation turnover rates are higher for Al_2O_3 than SiO_2 supports (4-fold higher at 453 K) for all MCH and H_2 pressures, indicating that these rate enhancements are similar at all MCH and H_2 pressures. On either support, MCH dehydrogenation turnover rates are insensitive to Pd nanoparticle size, as is the case also for their kinetic trends with MCH and H_2 pressure (eq 7). These data show that the binding properties of the ensembles of Pd-atoms that stabilize the relevant TS are unaffected by the size of the Pd nanoparticles dispersed on Al_2O_3 or SiO_2, a conclusion supported by the similar activation enthalpies measured on Pd/Al_2O_3 (64 ± 6 kJ/mol) and Pd/SiO_2 (65 ± 9 kJ/mol; discussed in Section 3.7 after a full derivation of the kinetic model is described, which involves the effect of the less reactive species). Such insensitivity to size is likely to reflect the significant coverages of less reactive MCH-derived species (denoted as X*) which form TOL much more slowly than other more reactive intermediates but occupy Pd surfaces. Such X* species form dense adlayers on Pd surfaces, leave the different coordinative unsaturation of surface Pd-atoms on small and large nanoparticles no longer accessible to reactants, and force MCH dehydrogenation events to occur on the interstices in the adlayers, which erases the most significant structural differences among differently sized nanoparticles.

Size-independent rates are typically observed for reactions on surfaces that are densely covered by strongly bound species derived from reactants, such as CO oxidation on Pt nanoparticles[30] and CO hydrogenation on Co nanoparticles,[31] which occur in the presence of dense CO* adlayers that weaken the structural features and intrinsic nonuniformity of small metal

https://doi.org/10.1021/acscatal.4c07240
ACS Catal. 2025, 15, 676−696

Scheme 3. Trend (the Solid Curve) of MCH Dehydrogenation Rate (r_{MCH}) versus Time on Stream (t); MCH Contacts Pd Catalysts at $t = t_0$, and r_{MCH} Starts to be Recorded at $t = t_s$ on Pd Surfaces Covered by the Less Reactive Species X*[a]

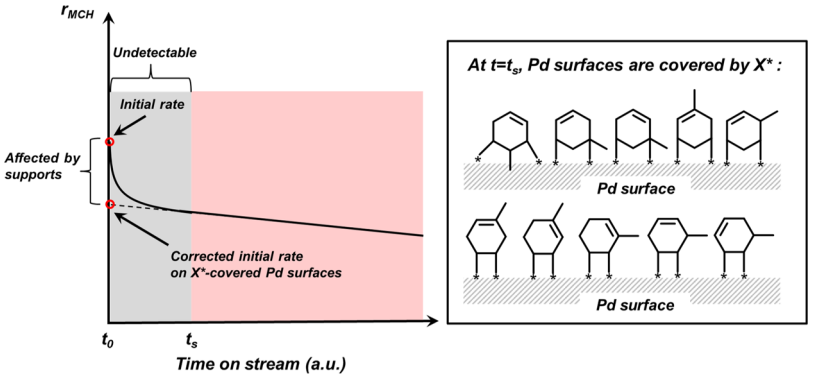

[a]The right panel depicts positional isomers of an illustrative family of bound intermediates with a given H-content ($TH_2(\gamma_2*)$); * denotes the surface attachment point through Pd−C bonds.

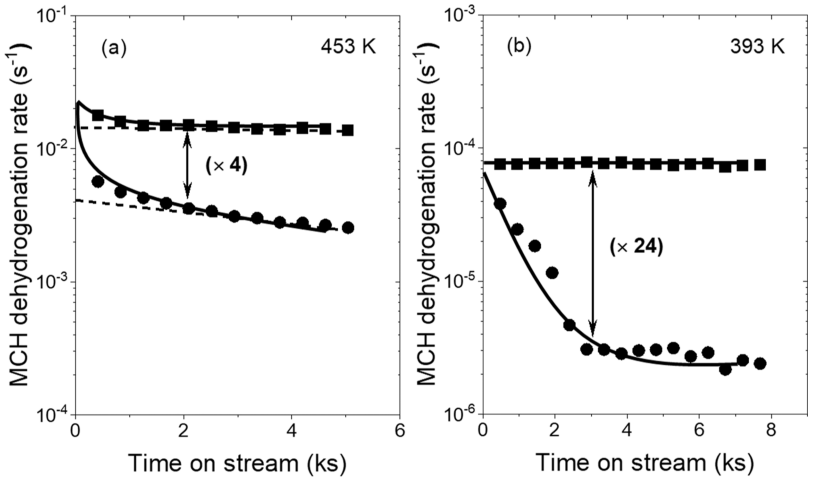

Figure 6. (a) MCH dehydrogenation rates versus time on stream at 1 kPa MCH, 4 kPa H_2, 453 K for Pd/Al_2O_3-2.1 (■) and Pd/SiO_2-11 (●) measured by a fast-screening GC method. (b) MCH dehydrogenation rates versus time on stream at 1 kPa MCH, 1 kPa H_2, 393 K for Pd/Al_2O_3-2.1 (■) and Pd/SiO_2-11 (●). Solid curves are used to guide the eye, and the dashed lines in Figure 6a represent corrections described in Section S1.2.

nanoparticles. This is also evident from alkane dehydrogenation and hydrogenolysis on Ir, Rh, Pt, and Ru catalysts on which dense adlayers form by dehydrogenated species with different locations of double bonds, metal−carbon attachment points, and H-content.[32,33]

The effects of MCH and H_2 pressure on dehydrogenation turnover rates (r_I; step I; Scheme 1) are shown in Figure 5 for Pd nanoparticles on Al_2O_3 and SiO_2, but also on MgO and CeO_2 supports. On all samples, these trends are accurately captured by the functional form of eq 7. Pd/CeO_2 and Pd/MgO showed 3.5 and 2.8 times higher MCH dehydrogenation turnover rates than Pd/SiO_2, respectively, at 453 K. An intra-aggregate intimate mixture of Pd/SiO_2 and (metal-free) Al_2O_3 showed rates about 1.5 times higher than Pd/SiO_2 (Figure S11, SI), indicating that Al_2O_3 effects on turnover rates do not require atomic contact with Pd nanoparticles; similar effects of Al_2O_3, as support or intra-aggregate mixtures, were previously reported for TOL hydrogenation rates on Pt nanoparticles, with mixtures of Pt/SiO_2 and Al_2O_3 giving TOL hydrogenation rates about 2.6 higher than Pt/SiO_2 at 393 K.[35] These support effects are similar for MCHE formation (r_I; step I; Scheme 1) and consumption (r_{II}; step II; Scheme 1), as evident from 1MCHE/MCH ratios that are similar on all supports at all MCH and H_2 pressures (Figure 3). The similar kinetic effects of MCH and H_2 pressures on turnover rates (Figure 5), the absence of detectable effects of Pd nanoparticle size (Figure 4), and the rate enhancements evident for Al_2O_3, CeO_2, and MgO (Figure 5), even without Pd nanoparticles in direct contact with Al_2O_3 (Figure S11) suggest that:

(i) supports do not enable new reaction channels, kinetically relevant elementary steps, or nanoparticle surfaces with different binding properties relevant for TOL formation from MCH or MCHE;

(ii) supports induce rate enhancements by allowing Pd nanoparticles to retain a larger fraction of their surfaces available for stabilizing the TS structures required for the most competent routes from MCH to TOL.

The next two sections examine these inferences for the specific case of Al_2O_3 as a noninnocent support through:

(i) initial rate transients that demonstrate the effects of support on the extent of accumulation of the less reactive species (X*);

(ii) the elimination of support-induced rate enhancements by titration of Lewis acid−base (LAB) pairs with propionic acid during MCH dehydrogenation;

https://doi.org/10.1021/acscatal.4c07240
ACS Catal. 2025, 15, 676−696

(iii) the relative reactivity of (metal-free) Al_2O_3 and SiO_2 for reactions of MCHE and MCHD, which act as plausible gaseous molecular shuttles between metal nanoparticles and support surfaces.

3.4. Evidence for the Role of Supports in Preserving Pd-Atom Ensembles Free of Less Reactive MCH-Derived Species during Dehydrogenation Catalysis. The concept of the less reactive MCH-derived species (denoted as X*) was mentioned earlier (Section 3.3) as species that form TOL much more slowly than the more competent intermediates that account for most MCH dehydrogenation turnovers. These species occupy bare atom ensembles, rendering them unavailable for more productive channels. These species reach their steady-state surface coverages upon initial contact with reactants, but over time scales longer than those required for turnovers through more competent intermediates. X* species accumulate during initial contact with reactants, leading to an initial decrease in rate and to steady-state X* coverages. Such processes differ from irreversible deactivation processes caused by unreactive organic residues.[51,52] X* can be removed via desorption or slow reactions that ultimately form TOL. The evolution of MCH dehydrogenation turnover rates (r_{MCH}) with time is depicted in Scheme 3, with t_0 denoted as the point of initial contact with reactants; this scheme also shows the illustrative examples of X* species (the right side of Scheme 3). Some of them can desorb as gaseous MCHE and MCHD intermediates, while others, because of their H-content and location are consumed only via slow elementary steps on Pd nanoparticles. The rates and kinetic trends on all catalysts (Figures 2, 4, and 5) were measured after this initial rate decrease ($t = t_s$); all reported rates are corrected for intervening changes in rate with time by extrapolation of initial and final rates at each condition (details in Section S1.2). Such rates, by intent and design, do not account for an initial decrease in rate that differs in extent among samples used in this work.

The dashed lines in Figure 6a show the correction to initial rates by the linear extrapolation after the initial decrease in rate (after 1.8 ks) on Pd/Al_2O_3 and Pd/SiO_2; these data were measured using chromatographic protocols that allowed sampling every 1.8 ks, and were able to isolate 1MCHE from MCH and TOL, but they cannot capture the initial transients in dehydrogenation turnover rates. Faster chromatographic protocols (~0.4 ks per sample) can detect such trends but cannot measure MCHE concentrations. The solid curves in Figure 6a are proposed to describe the above inference for the support effect and represent the trends for MCH dehydrogenation turnover rates on Pd/Al_2O_3 and Pd/SiO_2, which started at the same level but decreased much faster with time on Pd/SiO_2.

The data in Figure 6b show a decrease in dehydrogenation rates upon initial contact with reactants (at 393 K) that is much more evident on Pd/SiO_2 than Pd/Al_2O_3; MCH dehydrogenation turnover rates for Pd/SiO_2 and Pd/Al_2O_3 were the same at the beginning, but the approaches to steady-state are different for these two catalysts and account for the rate enhancements at steady-state (Figure 6b). The rate enhancement factor decreased from 24-fold at 393 K to 4-fold at 453 K, either because there are fewer X* species to scavenge at higher temperature as X* becomes more reactive, or SiO_2 supports become competent enough to remove X* species more efficiently. Species X* cannot be efficiently converted to TOL products, and they would reach steady-state coverages over time scales longer than characteristic turnover times, but shorter than those for deactivating species that are unreactive and account for deactivation but do not contribute to measured dehydrogenation turnover rates. The fact that species X* can desorb from Pd surfaces requires that X(g) should be closed-shell molecules, such as MCHE and MCHD, which can react on the support surfaces and presumably on the Lewis acid–base (LAB) pairs indicated by the titration experiments below.

The role of LAB pairs in the scavenging of desorbed forms of X* was confirmed by their titration with propionic acid during MCH dehydrogenation. Propionic acid (PA) was previously used to measure the number of LAB pairs during condensation and ketonization reactions on TiO_2 and ZrO_2.[46−49] Figure 7 shows the effect of introducing PA (2 Pa) on MCH dehydrogenation turnover rates on Pd/Al_2O_3-2.1 after reaching steady-state in the absence of PA (1 kPa MCH; 4 kPa H_2; 453 K). PA caused rates to decrease gradually to those measured on Pd/SiO_2, thus removing the rate enhancements conferred by the presence of Al_2O_3, indicating that LAB pairs are required for the observed support-mediated rate enhancements (Figure 5). Notably, the MCH dehydrogenation turnover rate on Pd/Al_2O_3 after removal of PA is still lower than the rate measured on Pd/SiO_2, which could be because SiO_2 is not inert and also contributes to the scavenging of the X* species. Similar effects of PA titration are evident for dispersed Pt nanoparticles in TOL hydrogenation; for all reactions, Al_2O_3, ZrO_2, and TiO_2 lead to higher rates than SiO_2 supports, but exposure to PA eliminates such support effects.[35] These support effects (for dehydrogenation and hydrogenation reactions) have been inaccurately attributed to the spillover of H atoms between metal and support functions; they reflect instead a role of LAB site pairs in scavenging less competent bound species (i.e., a subset of X* species) through their desorption and catalytic conversion at support LAB site pairs, thus preserving a larger fraction of nanoparticle surfaces accessible for the more competent reactive intermediates among the very diverse pool of bound species prevalent during these reactions.

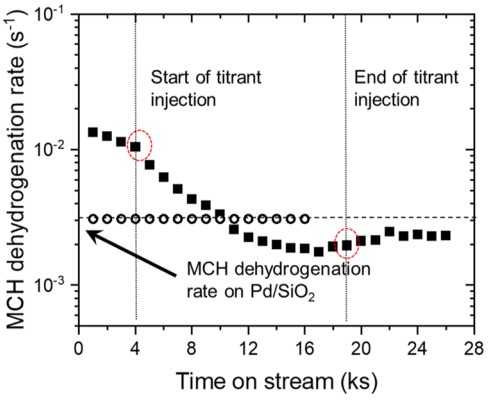

Figure 7. MCH dehydrogenation rates on Pd/Al_2O_3-2.1 (■) as a function of time on stream upon and after injection of propionic acid (453 K; 1 kPa MCH; 4 kPa; 2 Pa propionic acid). MCH dehydrogenation rates on Pd/SiO_2-5.7 (○) without propionic acid are added for comparison.

Some X* species may desorb as X(g) and be scavenged by support surfaces to form TOL (or molecules that form TOL more effectively than X* at Pd surfaces), thus decreasing X* coverages on Pd and increasing the prevalence of binding ensembles for more competent intermediates. These support-mediated reactions may be attributed to Lewis acid–base (LAB)

https://doi.org/10.1021/acscatal.4c07240
ACS Catal. 2025, 15, 676−696

pairs that may be more abundant or competent on Al_2O_3 than SiO_2 surfaces, as depicted in Scheme 4. MCH dehydrogenation

Scheme 4. Proposed Reaction Channels that Form and Consume Less Reactive Species (X*)[a]

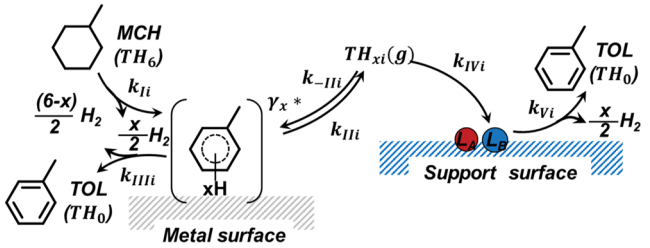

[a]The k_{ni} and k_{-ni} terms denote the forward and reverse kinetic constants for step n. The subscript x identifies species with $(6 - x)$ H-atoms removed from MCH, while i accounts for the presence of diverse isomers for X* species with a given number of H-atoms (Scheme 3). Unidirectional forward arrows denote irreversible steps; bidirectional arrows indicate reversible steps.

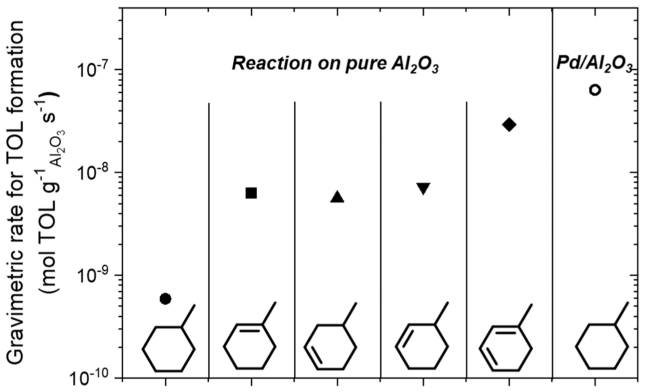

Figure 8. Gravimetric rate for TOL formation on Al_2O_3 at 453 K, 4 kPa H_2 and different combinations of 1 kPa MCH (●), 1 kPa MCH and 4 Pa 1MCHE (■), 1 kPa MCH and 4 Pa 3MCHE (▼), 1 kPa MCH and 4 Pa 4MCHE (▲), 1 kPa MCH and 4 Pa 1,4MCHD (◆). The gravimetric rate for TOL formation (○) on Pd/Al_2O_3-2.1 at 1 kPa MCH, 4 kPa H_2, 453 K.

events occur on Pd surfaces and form diverse positional isomers of bound species different in the location of their surface attachment;[52] such diversity is enabled by the relative reactivity of specific C−H bonds in subsequent H-abstractions from preceding intermediates and it is ubiquitous in the practice of hydrogenation-dehydrogenation reactions. Steps (I) and (III) represent the formation and conversion of X* on Pd and Step (II) represents their reversible desorption as closed-shell gaseous shuttles (e.g., MCHE, MCHD isomers). Steps (IV) and (V) depict the binding and reactions of these molecules at support surfaces. These processes, if they occurred at the requisite rates, would moderate steady-state X* coverages at Pd surfaces, thus retaining a larger fraction of the binding ensembles available for the more competent intermediates that account for most observed dehydrogenation turnovers. These proposals are considered in the next section by experiments that show that:

(i) such sites catalyze MCHE and MCHD (but not MCH) reactions;
(ii) the effects of temperature on support-mediated MCHE and MCHD reactions and their implications for the effects of temperature on the observed rate differences between Pd nanoparticles on Al_2O_3 and SiO_2 supports.

3.5. Methylcyclohexene and Methylcyclohexadiene Reactions on Metal-Free Al_2O_3 and SiO_2. The presence of LAB site pairs on oxide supports is required for the support-mediated rate enhancements shown in Figures 5 and 6 and the titration eliminates them. These sites are thought to act by scavenging desorbed species derived from X* (Figure 7). Such scavenging reactions do not contribute in a detectable additive manner to measured TOL formation rates; they contribute to measured rates by uncovering Pd ensembles for Pd-mediated turnover rates through more competent bound intermediates. The data in Figure 8 show TOL formation rates on Pd-free Al_2O_3 using MCH, MCH/MCHE, and MCH/MCHD reactants at 453−513 K. MCHE isomers and 1,4MCHD were mixed with 1 kPa MCH at partial pressures (4 Pa) much lower than those present during MCH dehydrogenation on dispersed Pd nanoparticles (10^{-3} Pa MCHE; $<10^{-17}$ Pa 1,4MCHD; for 1 kPa MCH, 4 kPa H_2, at 453 K). Therefore, even if Al_2O_3 can convert all MCHE and MCHD that egress from Pd surfaces at investigated conditions (453−553 K; 0.5−4 kPa MCH; 1−16 kPa H_2) to TOL, this contribution is still too low to account for the rate enhancement from Pd/SiO_2 to Pd/Al_2O_3 (Figure 5). As a result, additive dehydrogenation reactions of MCHE or MCHD on supports are not responsible for the observed rate enhancements.

1MCHE/H_2 reactants form TOL and MCH on (metal-free) Al_2O_3 and SiO_2 (Figure 9a). These products formed via disproportionation (MCH/TOL = 2) and dehydrogenation (TOL); measured MCH/TOL molar ratios in products are 0.3 on Al_2O_3 and 0.1 on SiO_2, consistent with the predominance of dehydrogenation routes. MCHE can only form TOL during MCH dehydrogenation on Pd catalysts, and they cannot be "scavenged" to form MCH on Al_2O_3 or SiO_2 supports because that would go in the wrong thermodynamic direction. The gravimetric consumption rates of MCHE on Al_2O_3 are over 3 times higher than those on SiO_2, indicating Al_2O_3 is more competent than SiO_2 in scavenging the desorbable X* species at 453 K.

Figure 9b shows 1MCHE conversion rates to TOL (per mass) on metal-free SiO_2 and Al_2O_3 at different temperatures in Arrhenius form. These rates are higher (about 3-fold) on Al_2O_3 than SiO_2, indicative of the relative number and competence of LAB site pairs in reactions of gaseous intermediates on these two supports. On both supports, rates increase with increasing temperature with the expected Arrhenius dependence. At 513 K, rates on SiO_2 reach values similar to those on Al_2O_3 at 453 K, suggesting that the smaller rate enhancements observed at higher temperatures (Figure 6) may reflect an increasing competence of SiO_2 surfaces in scavenging desorbed molecules derived from X*. X* species can only desorb as closed-shell structures, which then diffuse and react on support surfaces (even in physical mixtures). TOL can be ruled out as the scavenged species because it does not inhibit rates at investigated conditions in this work (Section S4, SI). Therefore, MCHE and MCHD isomers could act as molecular shuttles to communicate Pd and support surfaces.

3.6. Kinetic Consequences of Less Reactive Species X*. The specific C−H bond activation step that limits MCH dehydrogenation turnovers on Pd nanoparticles is not affected by their size (2−11 nm in diameter) or by the identity of the support (Al_2O_3, SiO_2, MgO, and CeO_2) (Sections 3.2 and 3.3), but LAB pairs on supports decrease the coverage of less reactive

https://doi.org/10.1021/acscatal.4c07240
ACS Catal. 2025, 15, 676−696

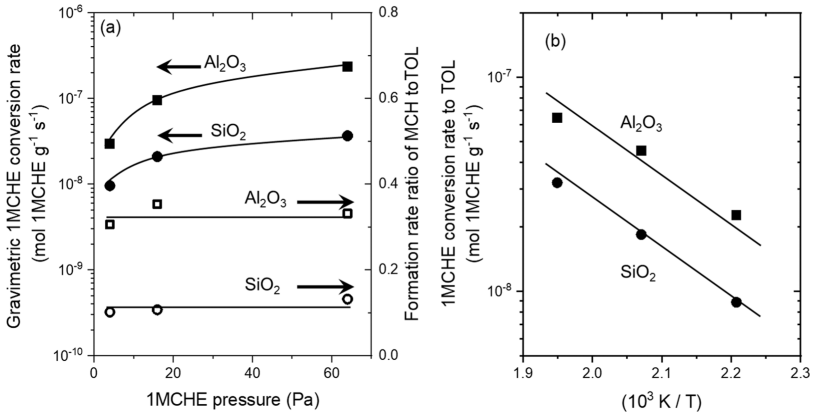

Figure 9. (a) Gravimetric 1MCHE conversion rate (summation rates for MCH and TOL formation) versus 1MCHE pressure measured on metal-free Al_2O_3 (■) and SiO_2 (●) at 4 kPa H_2; 453 K. Ratio of formation rate of MCH to TOL (4 kPa H_2; 453 K) measured on metal-free Al_2O_3 (□) and SiO_2 (○). (b) Gravimetric 1MCHE conversion to TOL rates (from dehydrogenation and disproportionation pathways) as a function of reciprocal temperature on metal-free Al_2O_3 (■) and SiO_2 (●) (453−513 K; 4 Pa 1MCHE; 4 kPa H_2). Solid curves and lines indicate the trends.

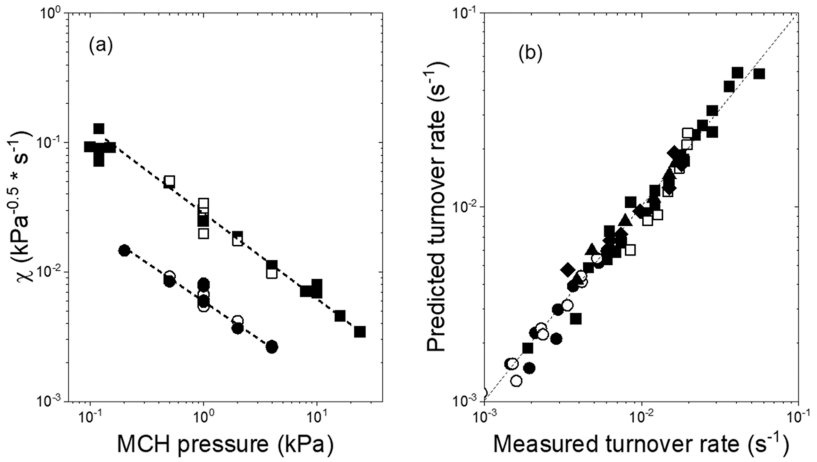

Figure 10. (a) χ (eq 18) as a function of MCH pressure on Pd/Al_2O_3-2.1 (■), Pd/Al_2O_3-6.3 (□), Pd/SiO_2-5.7 (●) and Pd/SiO_2-11 (○) at 453 K; χ for Pd/MgO and Pd/CeO_2 are not included here for clarity, and can be found in Figure S6. (b) Parity plots for MCH dehydrogenation rates at 453 K at 0.1−24 kPa MCH and 1−24 kPa H_2 on Pd/Al_2O_3-2.1 (■), Pd/Al_2O_3-6.3 (□), Pd/SiO_2-5.7 (●), Pd/SiO_2-11 (○), Pd/MgO-6.7 (▲), Pd/CeO_2-8.4 (◆).

X* species. The evidence and inferences presented in Sections 3.3−3.5 suggest that X* species that can desorb can react at LAB pairs on supports more effectively than on Pd nanoparticles. These lower X* coverages increase the number and size of the ensembles required to bind the kinetically relevant C−H activation TS within dense adlayers of MCH-derived species. The fractional coverage of these less reactive species (θ_{X^*}) depends on the identity of the support and must be considered in the site balance:

$$1 - \theta_{X^*} = \theta_* + \beta'[\mathrm{MCH}]\theta_*^{\gamma_s} \tag{17}$$

Here, γ_s is the number of contiguous Pd surface atoms required to bind the MASI, and β' is a lumped rate parameter that depends only on temperature. The $\beta'[\mathrm{MCH}]\theta_*^{\gamma_s}$ term accounts for the fractional coverage of the MASI, which was shown above not to depend on H_2 pressure (Figure 2b). For example, if $TH_6(\gamma_6{*})$ was the MASI, coverage of $TH_6(\gamma_6{*})$ should be $\gamma_6 K_{TH_6}[TH_6]\theta_*^{\gamma_6}$ (eq 10) with $\gamma_6 K_{TH_6}$ corresponding to β' and γ_6 corresponding to γ_s. Section S2.1 shows the derivation for the possible MASI species and their coverage can be expressed as $\beta'[\mathrm{MCH}]\theta_*^{\gamma_s}$.

A rearrangement of eq 7 leads to the definition of a term χ that accounts for the effects of MCH and H_2 pressures on rates

$$\chi = \frac{r_1\sqrt{[H_2]}}{[\mathrm{MCH}]} = \alpha'\theta_*^{\gamma_4+1} \ (\alpha' = \gamma_6 k_3 K_2 K_1 \sqrt{K_9}) \tag{18}$$

Derivative of θ_* with respect to [MCH] (eq 17) and derivative of χ with respect to θ_* (eq 18) can be combined to give

$$\frac{d\ln(\chi)}{d\ln([\mathrm{MCH}])} = -\frac{\frac{\gamma_4+1}{\gamma_s}}{\frac{1}{\gamma_s\beta'[\mathrm{MCH}]\theta_*^{\gamma_s-1}} + 1} \tag{19}$$

The data in Figure 10a show that $\ln(\chi)$ is a linear function of $\ln([\mathrm{MCH}])$ for all catalysts at 0.5−24 kPa MCH pressures, irrespective of the support identity. This requires the right side of eq 19 to be a constant and does not depend on MCH pressure, which requires

$$\gamma_s\beta'[\mathrm{MCH}]\theta_*^{\gamma_s-1} >> 1 \tag{20}$$

The absolute value of the slope in Figure 10a should be equal to $\frac{\gamma_4+1}{\gamma_s}$, reflecting the ratio of the occupied contiguous Pd surface

https://doi.org/10.1021/acscatal.4c07240
ACS Catal. 2025, 15, 676−696

Table 2. σ and δ from Rate Data Regression for All Pd Catalysts at 453 K[a]

catalyst	supports	mean Pd nanoparticle diameter (nm, TEM[b])	σ ($\times 10^2$ kPa$^{(\delta-1)/(0.5)}$ s^{-1})[c]	δ[c]
Pd/SiO_2-5.7	SiO_2	5.7(±0.6)	0.63(±0.06)	0.60(±0.18)
Pd/SiO_2-11	SiO_2	11(±1.1)	0.63(±0.03)	0.61(±0.28)
Pd/MgO-6.7	Al_2O_3	2.1(±0.3)	1.5(±0.1)	0.53(±0.14)
Pd/CeO_2-8.4	Al_2O_3	6.3(±1.0)	1.7(±0.2)	0.48(±0.28)
Pd/Al_2O_3-2.1	MgO	6.7(±0.6)	2.6(±0.1)	0.58(±0.02)
Pd/Al_2O_3-6.3	CeO_2	8.4(±1.4)	2.5(±0.3)	0.75(±0.40)

[a]Rate data are reported in Figures 2, 4, and 5; The errors indicate 95% confidence intervals. [b]Surface averaged diameter of Pd nanoparticles from TEM calculated with eq 1, Section 2.1. All micrographs can be found in Figure S2, SI. [c]From eq 22; $\sigma = \gamma_6 k_3 K_2 K_1 \sqrt{K_9}\left(\frac{1-\theta_{X^*}}{\beta'}\right)^{\delta}$, $\delta = \frac{\gamma_4+1}{\gamma_s}$.

atoms for the TS to those for the MASI for MCH dehydrogenation. Equations 17 (site balance equation) and 20 can be combined to give

$$\theta_* \ll \frac{\gamma_s}{\gamma_s+1}(1-\theta_{X^*}) < 1-\theta_{X^*} = \theta_* + \beta'[\mathrm{MCH}]\theta_*^{\gamma_s} \tag{21}$$

Equation 21 requires the available Pd-atom ensembles were densely covered by the reactive MCH-derived species for most conditions for MCH dehydrogenation in this work, and available Pd-atom ensembles were only sparsely covered at very low MCH pressure (lower than 0.15 kPa) where χ is independent of MCH pressure (Figure 10a). At all conditions, MCH dehydrogenation occurs on X*-covered Pd surfaces and θ_{X^*} cannot be neglected.

Equations 15, 17, and 21 represent the rate equation, site balance, and nontrivial coverage of the MASI, respectively. They are combined to give

$$r_1 = \sigma\frac{[\mathrm{MCH}]^{1-\delta}}{\sqrt{[\mathrm{H_2}]}}\left(\sigma = \gamma_6 k_3 K_2 K_1\sqrt{K_9}\left(\frac{1-\theta_{X^*}}{\beta'}\right)^{\delta}, \delta = \frac{\gamma_4+1}{\gamma_s}\right) \tag{22}$$

where σ is a lumped parameter affected by θ_{X^*} that depends on the identity of the support and temperature, and δ represents the ratio of the occupied contiguous Pd surface atoms for the TS to those for the MASI for MCH dehydrogenation. Figure 10b shows the parity plot for the predicted and measured MCH dehydrogenation turnover rates on all Pd catalysts at 453 K, and the corresponding parameters (σ and δ) are shown in Table 2. δ values (around 0.6) are similar for all Pd catalysts at investigated conditions. The data in Figures 5 and 6 suggest steady-state coverages of the less reactive species (θ_{X^*}) are affected by the identity of the support, which is consistent with the difference in apparent rate constant σ due to different θ_{X^*} term; and the other intrinsic rate or equilibrium constants depend only on binding properties of Pd nanoparticles, which are not affected by the identity of support and will be discussed in the following section (Section 3.7). Overall, the support effects on MCH dehydrogenation turnover rates are induced by different abilities in scavenging the less reactive species X* and affecting their steady-state coverages (θ_{X^*}) in the rate eq (eq 22).

3.7. Effects of the Less Reactive Species X* on the Activation Energy for MCH Dehydrogenation. The kinetic response of MCH dehydrogenation turnover rates to MCH and H_2 pressures (Figures 2 and 4), together with the functional form of eq 15, indicate that the removal of the second H-atom from MCH (step 3, Scheme 2) is the sole kinetically relevant step at 453 K and that all preceding steps are quasi-equilibrated. Transition state theory (TST) invokes a hypothetical equilibrium between reactants and an activated complex to describe the rates of each elementary step.[53] The lumping of all equilibrated elementary steps (Steps 1, 2, and 9; Scheme 2) leads to the transition state that mediates the cleavage of the C−H bond (Step 3; Scheme 2) on X*-covered Pd surfaces, reflected in the functional form of eq 15, gives the overall stoichiometric reaction. Here, $K^{\ddagger}$ is the transition state equilibrium constant for

$$TH_6 + \gamma_{TS}\,* \overset{K^{\ddagger}}{\rightleftharpoons} TH_5(\gamma_{TS}\,^*)^{\ddagger} + \frac{1}{2}H_2 \tag{23}$$

the formation of the TS ($TH_5(\gamma_{TS}*)^{\ddagger}$) and half of H_2 molecule by dehydrogenating TH_6 on an ensemble of γ_{TS} contiguous Pd surface atoms. TST[53] then gives an expression for the MCH dehydrogenation turnover rate (r_{MCH})

$$r_{MCH} = \frac{k_b T}{h}K^{\ddagger}\frac{[\mathrm{MCH}]}{\sqrt{[\mathrm{H_2}]}}\theta_*^{\gamma_{TS}} \tag{24}$$

Here, k_b and h are the Boltzmann and Planck constants, respectively; T is the absolute temperature; and [MCH] and [H_2] are the pressures for MCH and H_2, respectively. At MCH pressures below 0.15 kPa, dehydrogenation rates at 453 K increase linearly with MCH pressure (Figure 2a), indicative of small coverages by reactive MCH-derived intermediates. The site balance equation (eq 17) then becomes

$$1-\theta_{X^*} = \theta_* \tag{25}$$

and eqs 24 and 25 give the rate equation

$$r_{MCH} = \frac{k_b T}{h}(1-\theta_{X^*})^{\gamma_{TS}}K^{\ddagger}\frac{[\mathrm{MCH}]}{\sqrt{[\mathrm{H_2}]}} \tag{26}$$

Here, θ_{X^*} represents the coverage of X*, the less reactive bound species, which is influenced by the scavenging support-mediated reactions proposed in Section 3.4. Such coverages can be directionally inferred from the initial decrease in rates upon contact with reactants (Figure 6), but cannot be determined directly. The θ_{X^*} term prevents unequivocal measurements of $K^{\ddagger}$ and therefore of the true turnover rates, which are reported here on the basis of the number of exposed Pd surface atoms before MCH reactions.

The transition state equilibrium constant ($K^{\ddagger}$) depends on the activation free energy ($\Delta G^{\ddagger}$)

$$K^{\ddagger} = \exp\left(\frac{-\Delta G^{\ddagger}}{RT}\right) = \exp\left(\frac{-\Delta H^{\ddagger} + T\Delta S^{\ddagger}}{RT}\right) \tag{27}$$

https://doi.org/10.1021/acscatal.4c07240
ACS Catal. 2025, 15, 676−696

$\Delta G^{\ddagger}$, $\Delta H^{\ddagger}$, $\Delta S^{\ddagger}$ are the free energy, enthalpy, and entropy involved in forming the transition state from its relevant precursors (in this case, a gaseous MCH molecule and an ensemble of γ_{TS} bare atoms with the release of 1/2 H_2), leading to a logarithmic relation between rates and reciprocal temperatures

$$\ln(r_{eff}) = -\frac{\Delta H^{\ddagger}}{R}\frac{1}{T} + \gamma_{TS} \times \ln(1 - \theta_{X^*}) + \frac{\Delta S^{\ddagger}}{R}$$
$$\left(r_{eff} = \frac{r_{MCH} h \sqrt{[H_2]}}{k_b T [MCH]}\right) \quad (28)$$

The "effective" MCH dehydrogenation rate (r_{eff}) is defined as $\frac{r_{MCH} h \sqrt{[H_2]}}{k_b T [MCH]}$. This equation shows that activation enthalpies can be measured from r_{MCH} values at different temperatures, only when θ_{X^*} is insensitive to temperature change in the measurement (even if its magnitude is unknown). Values of r_{MCH} measured at each temperature on fresh catalysts would lead to different θ_{X^*} values at each temperature because the initial approach to steady-state for X* depends on the temperature, as shown from the strong effects of temperature effect on the rate enhancements (Figure 6).

The effects of temperature on rates were assessed by initial rate measurements at 463 K (0.08 kPa MCH, 4 kPa H_2) to establish a given X* coverage and the temperature decreased to 443 K (at 0.005 K/s) and then increased rapidly to 463 K and held for 1 h. This protocol with proper corrections would render all reported MCH dehydrogenation turnover rates with the same θ_{X^*} that was already set by the approach to steady-state at 463 K. The detailed procedures and rate data as a function of temperature are shown in Figures S12 and S13 (SI).

The data in Figure 11 show r_{eff} values as a function of reciprocal temperature on Pd/Al_2O_3 and Pd/SiO_2; the slope of the regressed lines represents the value of $-\frac{\Delta H^{\ddagger}}{R}$, while the intercept gives the value of $\gamma_{TS} \times \ln(1 - \theta_{X^*}) + \frac{\Delta S^{\ddagger}}{R}$. The value of this intercept depends on the activation entropy, the number

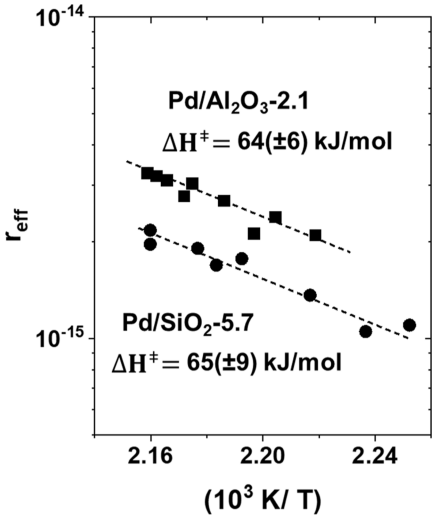

Figure 11. Effective MCH dehydrogenation turnover rates (r_{eff}; eq 28) as a function of reciprocal temperature on Pd/Al_2O_3-2.1(■) and Pd/SiO_2-5.7(●) (0.08 kPa MCH, 4 kPa H_2). The dashed lines represent linear regression.

of contiguous Pd surface atoms required to bind the kinetically relevant transition state (γ_{TS}), and the value of θ_{X^*}; neither γ_{TS} nor θ_{X^*} are independently measurable and θ_{X^*} depends on the identity of the support, thus precluding an assessment of activation entropies. Measured activation enthalpies for MCH dehydrogenation on Pd/Al_2O_3 and Pd/SiO_2 are identical within experimental uncertainty (64(±6) kJ/mol and 65(±9) kJ/mol, respectively), indicating that the intrinsic binding properties of Pd nanoparticle surfaces are unaffected by the Al_2O_3 and SiO_2 supports, as also evident from kinetic trends (Figures 2 and 4) and rate equations (eq 15) that are similar for both supports. Supports affect MCH dehydrogenation turnover rates on Pd nanoparticles only through their consequences for the θ_{X^*} term in eq 26 (as discussed in Sections 3.4−3.5); these effects are mediated through the catalytic conversion of desorbable X* species on LAB site pairs and decreasing steady-state θ_{X^*} on Pd surfaces, as is also shown for toluene hydrogenation on Pt catalysts.[35]

3.8. Effects of the Less Reactive Species X* on Rate Enhancements for MCH Dehydrogenation. The results and inferences described in Sections 3.2−3.7 have led to the conclusion that support effects reflect the scavenging of X* species through their conversion to products that bind less weakly at Pd ensembles during steady-state MCH dehydrogenation reactions. Other factors, such as support or metal identity and temperature may also affect X* coverages and the competence of metal and support surfaces for the conversion of X*-derived species. This section described a general framework for inferring the relative importance of such effects, through the development of a kinetic network for the formation and consumption of X*.

Scheme 3 (Section 3.4) depicts the decreases of MCH dehydrogenation turnover rates with time on stream due to the accumulation of X* on Pd surfaces and their reaction at metal surfaces and on supports (after desorption, Scheme 4). Plausible desorbed versions of X* are denoted as TH_{xi}, with the subscript i indicating positional isomers of TH_x (Scheme 4). These TH_x isomers desorb from Pd surfaces and reach LAB pairs on supports, where they react, thus preventing their readsorption and titration of Pd ensembles. There can be several such desorbable species, but the formalism proposed considers only a representative TH_x, which is consumed on supports at the rate of step V (Scheme 4)

$$r_V = \frac{k_V k_{IV}}{k_{-IV} + k_V}[TH_x]\theta_S \quad (29)$$

$[TH_x]$ is the pressure of the desorbed form of X*, θ_S is fractional coverage of LAB pairs which are accessible to $TH_x(g)$, and the k_n terms are the rate constants for each step in Scheme 4. These constants are grouped into one term (φ)

$$\varphi = \frac{k_V k_{IV}}{k_{-IV} + k_V} \quad (30)$$

that accounts for the competence of LAB pairs in scavenging reactions. The formation of the less reactive stranded species $TH_x(\gamma_x{}^*)$ is assumed to proceed via similar types of H-abstraction reactions as the kinetically relevant step for the more reactive ones that account for MCH dehydrogenation turnovers on Pd surfaces at 453 K. When gaseous $TH_x(g)$ and bound $TH_x(\gamma_x{}^*)$ species are present at pseudo steady-state (PSS), their rates of formation and consumption are the same. PSS assumption for $TH_x(g)$ gives

https://doi.org/10.1021/acscatal.4c07240
ACS Catal. 2025, 15, 676−696

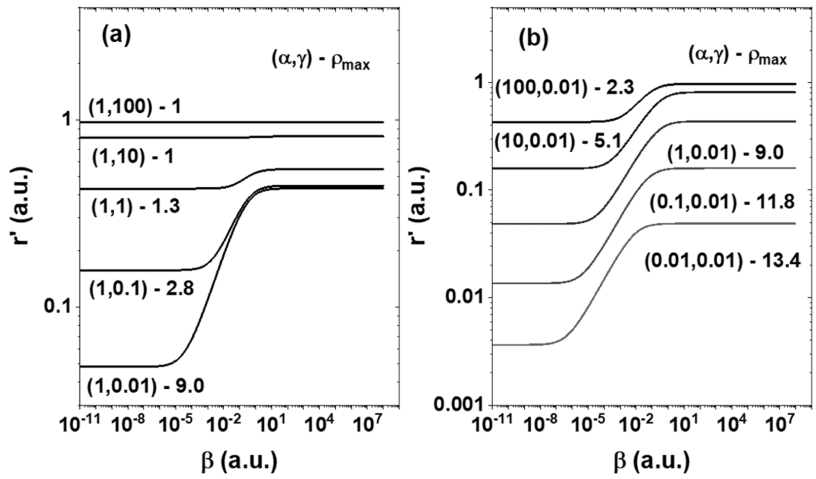

Figure 12. (a) Nondimensionalized MCH dehydrogenation turnover rate (r') as a function of β (eq 37), at a given α (eq 35; the ratio of the desorption rate to the formation rate of the less reactive species on metal surfaces) but different γ (eq 36; the ratio of the consumption rate to desorption rate of the less reactive species on metal surfaces). (b) Nondimensionalized MCH dehydrogenation rate (r') as a function of β at a given γ but different α.

$$\varphi[\mathrm{TH}_x(\mathrm{g})]\theta_S = k_{II}\theta_{\mathrm{TH}_x(\gamma_x^*)} - k_{-II}[\mathrm{TH}_x(\mathrm{g})]\theta_*^{\gamma_x} \quad (31)$$

PSS assumption for $\mathrm{TH}_x(\gamma_x*)$ gives

$$k_I\frac{[\mathrm{MCH}]}{\sqrt{[\mathrm{H}_2]}}\theta_*^{\gamma_x} = k_{IV}[\mathrm{TH}_x(\mathrm{g})]\theta_S + k_{III}\frac{\theta_{\mathrm{TH}_x(\gamma_x^*)}}{\sqrt{[\mathrm{H}_2]}} \quad (32)$$

$\theta_{\mathrm{TH}_x(\gamma_x^*)}$ is the coverage of $\mathrm{TH}_x(\gamma_x*)$ species on Pd surfaces, θ_* is the coverage of unoccupied Pd-atoms. And site balance of the Pd surfaces during MCH dehydrogenation at low MCH pressure can be expressed as

$$1 = \theta_* + \theta_{\mathrm{TH}_x(\gamma_x^*)} \quad (33)$$

Equations 31−33 are combined to give

$$\frac{\theta_*^{\gamma_x}}{1-\theta_*} = \alpha\left(\frac{\beta}{\beta + \theta_*^{\gamma_x}} + \gamma\right) \quad (34)$$

$$\alpha = \frac{k_{II}\sqrt{[\mathrm{H}_2]}}{k_I[\mathrm{MCH}]} \quad (35)$$

$$\gamma = \frac{k_{III}}{k_{II}\sqrt{[\mathrm{H}_2]}} \quad (36)$$

$$\beta = \frac{\varphi\varepsilon}{k_{-II}} \quad (37)$$

$$\varepsilon = \frac{\theta_S}{\theta_*} \quad (38)$$

Here, α is the ratio of the desorption rate to the formation rate of the less reactive species on metal surfaces; γ accounts for the ratio of the consumption rate to desorption rate of the less reactive species on metal surfaces; β denotes the ratio of reactive scavenging rates of TH_x on support surfaces to their readsorption rates onto metal surfaces; ε is the ratio of θ_S to θ_* in a given catalyst sample. Notably, the θ_S term involved in ε is determined based on the accessible LAB pairs that are reachable via diffusion of TH_x. Directionally, the steady-state X* coverages would decrease as α, β or γ increase.

The nondimensional form of the rate equation (eq 7) relates the dimensionless rate (r') to the probability of finding the ensembles of γ_{TS} contiguous bare atoms required to stabilize the kinetically relevant TS ($\sim\theta_*^{\gamma_{TS}}$)

$$r' = \frac{r_I\sqrt{[\mathrm{H}_2]}}{k_{MCH}[\mathrm{MCH}]} = \theta_*^{\gamma_{TS}} \quad (39)$$

where k_{MCH} is the lumped rate constant, an intrinsic property of the nanoparticle surfaces. The results shown in Table 2 indicate that the ratio $\left(\delta = \frac{\gamma_4+1}{\gamma_s}\right)$ of number of contiguous ensembles required to bind the TS (γ_4 + 1; or γ_{TS}) for MCH dehydrogenation requires a different number of Pd sites compared to the MASI (γ_s), and the corresponding site ratio is about 0.6. Here, the absolute number of Pd-atoms for the ensembles are unknown, and only the relation can be obtained from kinetic measurements (Table 2). The less reactive species $\mathrm{TH}_x(\gamma_x*)$ are considered to require ensembles similar in size to those for the MASI (γ_s), thus, leading to the ratio of γ_{TS} (eq 39) to γ_x (eq 34) as 0.6 as well. For any given α and γ, which reflect the intrinsic properties of the metal nanoparticle, eqs 34 and 39 indicate that r' depends only on β, a parameter that depends solely on the identity, surface area, LAB site density, and the intrinsic reactivity of these sites of a given support.

Figure 12 shows that r' values increase monotonically as β increases for all α and γ values, because larger β (the ratio of scavenging rates of TH_x on support surfaces to their readsorption rates onto metal surfaces) means more competent supports that scavenge TH_x more efficiently. In the asymptotic limits of large and small β values, determined by the properties of the supports, rates become insensitive to such values. For any given metal, values of α and γ are fixed because they are determined by the formation, desorption, and consumption rates of the less reactive species on metal surfaces. When β is much larger than $\theta_*^{\gamma_x}$, desorption of the less reactive species (step II; Scheme 4) becomes irreversible, and TH_x reacts on support surfaces much more frequently than it readsorbs on nanoparticle surfaces. In this limit, rates reach their maximum values at nanoparticles surfaces (set by α and γ) and more competent supports cannot further increase rates. When β is much smaller than $\theta_*^{\gamma_x}$, the functional form of eq 34 indicates desorption of the less reactive species (step II; Scheme 4) becomes equilibrated because the supports are so inert that TH_x

https://doi.org/10.1021/acscatal.4c07240
ACS Catal. 2025, 15, 676−696

does not react on support surfaces at all, which corresponds to the minimum dehydrogenation rates.

For any given α (eq 35) and γ (eq 36) value, rate enhancement (ρ) is defined as

$$\rho = \frac{r'_{\beta}}{r'_{\beta\to 0}} \tag{40}$$

And a maximum value (ρ_{max}) is given by the two asymptotic limits in Figure 12

$$\rho_{max} = \frac{r'_{\beta\to\infty}}{r'_{\beta\to 0}} \tag{41}$$

Figure 12 also shows ρ_{max} at different values of α and γ. For any given α (Figure 12a), ρ_{max} decreases as γ increases and rate enhancement disappear ($\rho_{max} = 1$) when γ is large enough. The functional form of eq 34 indicates when γ is much larger than unity, the term involving support properties $\left(\frac{\beta}{\beta+\theta_*^{\gamma_{TS}}}\right)$ is canceled out. This case indicates TH_x reacts on metal surfaces much more frequently than it desorbs, corresponding to high activity of metal for scavenging TH_x. For any given γ (Figure 12b), ρ_{max} decreases as α increases. The functional form of eq 34 requires that θ_* approach unity when α approaches infinity, and the dimensionless rate (eq 39) of MCH dehydrogenation reaches the maximum. This case indicates TH_x desorbs much faster than it forms on metal surfaces.

This kinetic network also informs about how temperature affects the magnitude of the support-mediated rate enhancements, as shown by the data in Figure 6. MCH dehydrogenation rate enhancements (Pd/Al_2O_3 vs Pd/SiO_2) decrease with increasing reaction temperature, because both Al_2O_3 and SiO_2 supports become sufficiently competent as temperatures increase (Figure 9b), corresponding to larger β in Figure 12, and their corresponding r' move to the right along the curves in Figure 12, resulting in a smaller difference between r' for Pd/Al_2O_3 and Pd/SiO_2. An alternative proposal is Pd becomes more competent in removing TH_x by more efficient catalytic conversion or desorption on metal surfaces, corresponding to increased γ (Figure 12a) or α (Figure 12b), which would lead to smaller rate enhancement (ρ_{max}).

The contour plot in Figure 13 shows the values of ρ_{max} achievable through changes in the metal properties (α, γ) as the support properties change between its asymptotic limits. The ρ_{max} values (eq 41) are smaller than 1.2 at larger α (eq 35) or γ (eq 36) values, corresponding to the top region of Figure 13, representing situations where metal nanoparticles are intrinsically competent at reacting X*, thus requiring no assistance by support LAB sites. The bottom region in Figure 13 represents situations where metal nanoparticles are not competent in removing X*, and LAB sites on support can help by scavenging X(g) desorbed from metal surfaces. The support-induced rate enhancements on Pd catalysts in this work suggest the catalysts fall into the middle of the curves in Figure 12, or the bottom area of Figure 13. Rates of MCH dehydrogenation increase following the order of Pd/SiO_2, Pd/MgO, Pd/CeO_2, and Pd/Al_2O_3 because of increasing β (eq 37), affected by the capability of the support to scavenge the less reactive species as a consequence of different LAB pairs. This analysis and treatment can potentially be applied to other transition metals (e.g., Pt and Ni) at different temperatures for alkane dehydrogenation reactions for the rate enhancement effect induced by the supports.

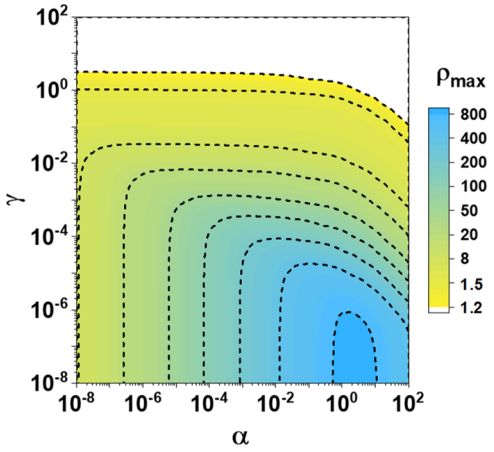

Figure 13. Maximum rate enhancement factor (ρ_{max}; eq 41) as a function of α (eq 35; the ratio of the desorption rate to the formation rate of the less reactive species on metal surfaces) and γ (eq 36; the ratio of the consumption rate to desorption rate of the less reactive species on metal surfaces).

3.9. Effects of Temperature on the Reversibility and Kinetic Relevance of H-Abstraction Steps. The data in Figure 1 at 453 K indicate that 1MCHE was at pseudosteady-state and that the approach to equilibrium for 1MCHE formation was much smaller than unity at all temperatures (Figure S8, SI), suggesting that MCH conversion to TOL is limited by elementary steps that precede MCHE formation (step I, Scheme 1) at 453−553 K. The data in Figure 14a show that MCH dehydrogenation rates (r_I; Scheme 1) on Pd/Al_2O_3-2.1 increase linearly at first and then sublinearly with increasing MCH pressure at 553 K. The data in Figure 14b show that MCH dehydrogenation rates are unaffected by H_2 pressure (2−16 kPa H_2) at each MCH pressure (at 0.16, 1, and 4 kPa MCH; 553 K;), leading to a rate equation of the form

$$r_I = k_{MCH}[MCH]\theta_*^{\gamma_{TS}} \tag{42}$$

with [MCH] as the MCH pressure, γ_{TS} as the number of contiguous Pd surface atoms required to bind the TS that mediates the kinetically relevant step for MCH dehydrogenation to MCHE; θ_* is the fraction of the Pd surface atoms that remain bare during reaction and k_{MCH} is the lumped rate and thermodynamic parameters that define the apparent rate constant. The curves in Figure 14 represent the regression of all rate data to the functional form of eq 42 with θ_* as a single-valued function of MCH pressure (and independent of H_2 pressure) and accurately describe all rate data. The functional form of eq 42 requires a kinetically relevant TS for MCHE formation (step I, Scheme 1) contains the same H-atoms as the MCH reactant molecules. Therefore, MCH dehydrogenation rates must be limited by the first H-abstraction step from bound MCH species 553 K, which precedes the second H-abstraction step that limited such rates at 453 K.

MCHE concentrations are determined by the relative rates of their formation (r_I; Scheme 1) and consumption (r_{II}; Scheme 1) rates. The kinetic trends of each rate with MCHE, MCH, and H_2 determine the prevalent MCHE pressures at steady-state and the identity of the elementary steps that limit MCHE conversion to TOL (step II; Scheme 1). 1MCHE/MCH ratios were essentially independent of both MCH and H_2 pressures at 453 K (Figure 3)

https://doi.org/10.1021/acscatal.4c07240
ACS Catal. 2025, 15, 676−696

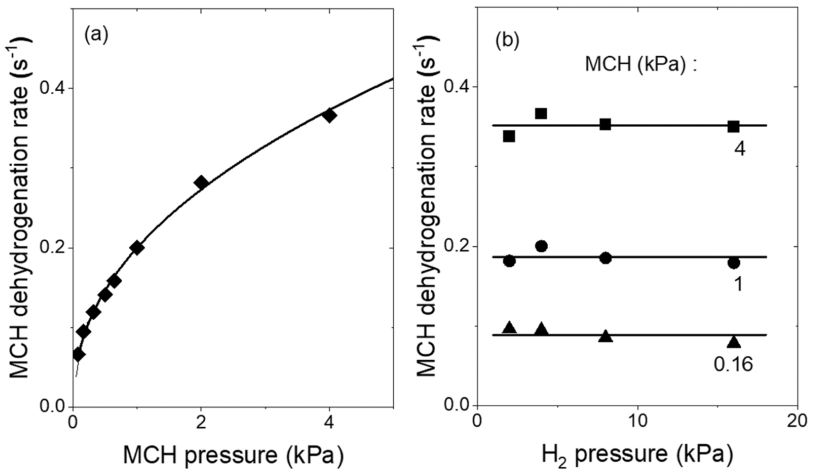

Figure 14. MCH dehydrogenation rates on Pd/Al_2O_3-2.1 as a function of MCH pressure (a, 4 kPa H_2) and H_2 pressure (b, at different MCH pressures, 4 kPa (■), 1 kPa (●) and 0.16 kPa (▲)) at 553 K. Solid curves and lines represent the regression of the rate data to the functional form of eq 42.

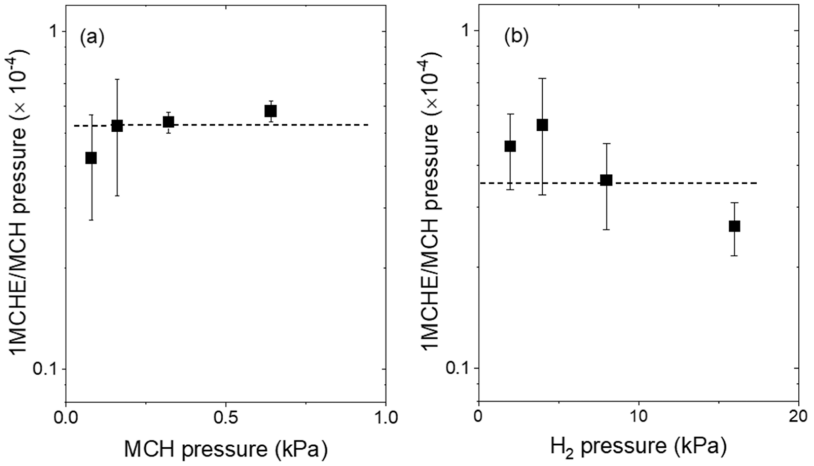

Figure 15. 1MCHE/MCH pressure ratios at 553 K on Pd/Al_2O_3-2.1 at (a) 4 kPa H_2 and (b) 0.16 kPa MCH. The dashed line indicates the trend.

and also at 553 K (Figure 15). Therefore r_I and r_{II} must be affected similarly by the H_2 pressure and the kinetically relevant TS for MCH dehydrogenation to MCHE and MCHE conversion to TOL must require binding ensembles that are similar in size, and θ_* is a single-valued function of MCH pressure. MCHE conversion rates are therefore described by

$$r_{II} = k_{MCHE}[MCHE]\theta_*^{\gamma_{TS}'} \quad (43)$$

where γ_{TS}' is the number of contiguous bare Pd surface atoms required to bind the kinetically relevant TS for MCHE conversion to TOL (step II; Scheme 1) and k_{MCHE} is the lumped rate and thermodynamic parameters that give the apparent rate constant for this conversion. Equations 42 and 43 can be combined to give

$$\frac{[MCHE]}{[MCH]} = \frac{k_{MCH}}{k_{MCHE}}\theta_*^{\gamma_{TS}-\gamma_{TS}'} \quad (44)$$

The data in Figure 14 show that θ_* depends on MCH but not on H_2 pressure at 553 K, while Figure 15 shows that the right side of eq 44 does not depend on MCH pressure. Consequently, the size of the ensembles required to bind the TS is the same ($\gamma_{TS}' = \gamma_{TS}$) for the steps that limit MCH dehydrogenation to MCHE (step I; Scheme 1) and MCHE conversion to TOL (step II; Scheme 1). The functional form of eq 43 requires that the TS for the kinetically relevant step in MCHE conversion to TOL (step II; Scheme 1) has the molecular composition of a MCHE molecule, indicating that the first H-abstraction from MCHE limits the rate of Step II (Scheme 1). As in the case of step I, the limiting H-abstraction step for step II shifts from the second to the first H-abstraction from MCHE as the temperature increases from 453 to 553 K.

The elementary steps proposed in Scheme 2 to describe the data (Figure 14) and to derive the rate equation (eq 15) at 453 K remain valid for MCH dehydrogenation reactions at 553 K, but with a shift in the kinetically relevant step. The data in Figure 14 suggest that the removal of the first H-atom from TH_6 is the kinetically relevant step (step 2; Scheme 2). Step 1 (MCH adsorption) must be quasi-equilibrated and the equation for MCH conversion to MCHE (r_I) becomes

$$r_I = \alpha'[MCH]\theta_*^{\gamma_S+1} \ (\alpha' = k_2K_1) \quad (45)$$

with γ_S denoting the number of contiguous Pd-atoms required to bind TH_S. A term χ' (553 K) is introduced to capture the influence of MCH and H_2 pressures on MCH dehydrogenation rates

$$\chi' = \frac{r_I}{[MCH]} = \alpha'\theta_*^{\gamma_S+1} \ (\alpha' = k_2K_1) \quad (46)$$

https://doi.org/10.1021/acscatal.4c07240
ACS Catal. 2025, 15, 676−696

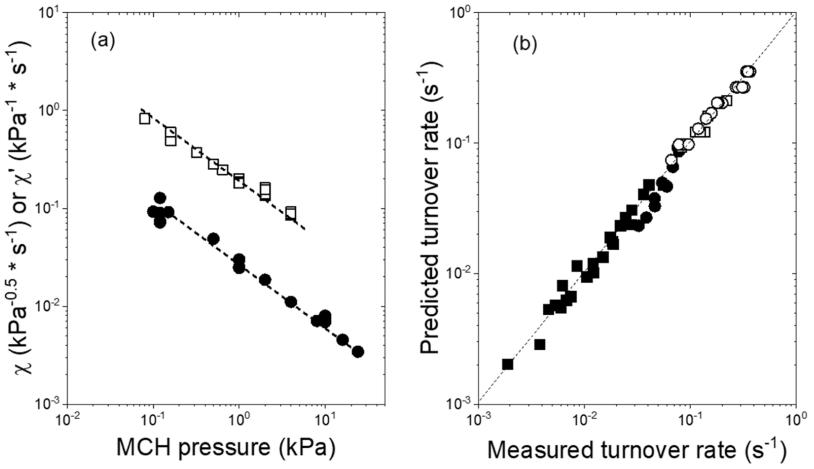

Figure 16. (a) Values of χ (eq 18) or χ' (eq 46) as a function of MCH pressure on Pd/Al_2O_3-2.1 at 453 K (●) and 553 K (□). χ or χ' at 483 and 513 K are not included here for clarity in this Figure but are shown in Figure S6 of the SI. (b) Predicted and measured for MCH dehydrogenation turnover rates for Pd/Al_2O_3-2.1 (0.1−24 kPa MCH and 1−24 kPa H_2) at 453 K (■), 483 K (●), 513 K (□), and 553 K (○).

Derivative of θ_* with respect to [MCH] (eq 17) and derivative of χ' with respect to θ_* (eq 46) can be combined to give

$$\frac{d\ln(\chi')}{d\ln([MCH])} = -\frac{\frac{\gamma_s+1}{\gamma_s}}{\frac{1}{\gamma_s\beta'[MCH]\theta_*^{\gamma_s-1}}+1} \quad (47)$$

in which the right-hand side depends only on MCH pressure and is independent of H_2 pressure. Figure 16a shows $\ln\chi$ (eq 18; 453 K) and $\ln\chi'$ (eq 46; 553 K), which account for the effects of MCH and H_2 pressures on rates, are single-valued linear functions of ln([MCH]) (1−24 kPa H_2) on Pd/Al_2O_3-2.1 at both temperatures. Such linear trends require the right side of eq 47 is a constant and does not depend on MCH pressure

$$\gamma_s\beta'[MCH]\theta_*^{\gamma_s-1} >> 1 \quad (20)$$

Equation 17 (site balance equation) and 20 can be combined to give

$$\theta_* \ll \frac{\gamma_s}{\gamma_s+1}(1-\theta_{X^*}) < 1-\theta_{X^*} = \theta_* + \beta'[MCH]\theta_*^{\gamma_s} \quad (21)$$

Equations 45, 17, and 21 represent the rate equation, site balance, and significant coverages of the MASI, respectively, at 553 K, which can be combined to give

$$r_1 = \sigma'[MCH]^{1-\delta}\left(\sigma' = k_2K_1\left(\frac{1-\theta_{X^*}}{\beta'}\right)^{\delta}, \delta = \frac{\gamma_5+1}{\gamma_s}\right) \quad (48)$$

Figure 16b compares measured MCH dehydrogenation turnovers with those predicted from eq 22 (at 453 and 483 K) and eq 48 (at 513 and 553 K) using the regressed σ, σ', and δ values listed in Table 3. The δ values (0.6) are similar at all temperatures on Pd/Al_2O_3-2.1, which reflects the ratio for the number of Pd-atoms required for the TS (γ_4 + 1 or γ_5 + 1) and the MASI (γ_s) (Table 2).

The shift in the kinetically relevant step from the second to the first H-abstraction step for both MCH (r_I, Scheme 1) and MCHE (r_{II}; Scheme 1) as temperature increases are reflected in the different H_2 terms for eqs 7 and 8 at 453 K and eqs 42 and 43 at 553 K. At 453 K, the abstraction of the first H atom from MCH is quasi-equilibrated, which requires the reverse rate of step 2 (H-addition to $TH_5(\gamma_5*)$; Scheme 2) is much larger than the forward rate of step 3 (H-abstraction of $TH_5(\gamma_5*)$; Scheme 2)

$$r_{-2} \geq r_3 \quad (49)$$

As temperature increased from 453 to 553 K, endothermic H-abstraction became more favored than exothermic H-addition, making the reverse rate of step 2 (H-addition to $TH_5(\gamma_5*)$; Scheme 2) much smaller than forward rate of step 3 (H-abstraction of $TH_5(\gamma_5*)$; Scheme 2)

$$r_{-2} \leq r_3 \quad (50)$$

Equation 50 suggests step 2 (H-abstraction to $TH_6(\gamma_6*)$; Scheme 2) is irreversible and becomes kinetically relevant at high temperatures.

In this work, we take MCH dehydrogenation on Pd nanoparticles as a model reaction and demonstrate a rigorous way for kinetic measurements for reactions with deactivating behaviors due to the accumulation of the less reactive species X*. The shift in the kinetically relevant step as temperature changes, the absence of a particle size effect on MCH dehydrogenation turnover rates, and rate enhancements induced by supports can be broadly applied to dehydrogenation

Table 3. Values of σ (Equation 22) or σ' (Equation 48) and δ (Equations 22 and 48) from Data in Figures 16a and S6 to Equations 22 and 48 for Pd/Al_2O_3-2.1 at All Temperatures[a]

catalyst[b]	reaction temperature (K)	σ(×10 kPa$^{(\delta-1)/(0.5)}$ s^{-1}[c]	δ[c]
Pd/Al_2O_3-2.1	453	0.26(±0.01)	0.58(±0.02)
Pd/Al_2O_3-2.1	483	1.4(±0.2)	0.73(±0.61)
catalyst[b]	reaction temperature (K)	σ'(×10 kPa$^{\delta-1}$ s^{-1})[d]	δ[d]
Pd/Al_2O_3-2.1	513	1.2(±0.1)	0.59(±0.12)
Pd/Al_2O_3-2.1	553	2.0(±0.1)	0.55(±0.02)

[a]Rate data are reported in Figures 16a and S6; The uncertainties listed represent 95% confidence intervals. [b]Pd/Al_2O_3-2.1 represents Pd nanoparticles with mean diameter of 2.1 nm dispersed on Al_2O_3 support. [c]From eq 22; $\sigma = \gamma_6k_3K_2K_1\sqrt{K_9}\left(\frac{1-\theta_{X^*}}{\beta'}\right)^{\delta}$, $\delta = \frac{\gamma_4+1}{\gamma_s}$. [d]From eq 48; $\sigma' = k_2K_1\left(\frac{1-\theta_{X^*}}{\beta'}\right)^{\delta}$, $\delta = \frac{\gamma_5+1}{\gamma_s}$.

https://doi.org/10.1021/acscatal.4c07240
ACS Catal. 2025, 15, 676−696

reactions on various metal catalysts other than Pd. The findings and analysis method in this work are informative to any catalyst with deactivating behaviors due to site blockage, which is not only limited to dehydrogenation reactions, but also common in hydrogenolysis, alkane cracking, and hydrocarbon reforming.

4. CONCLUSIONS

Methylcyclohexane (MCH) dehydrogenates on Pd nanoparticles (2.1−11 nm) to produce toluene (TOL) and release H_2, involving two stages from MCH to methylcyclohexene (MCHE) and then to TOL. The rates for the two stages are accurately described over wide ranges of temperatures, pressures, and coverages by rate expressions derived from a series of plausible elementary steps. MCHE intermediates form irreversibly at rates equal to their conversion rates to TOL at pseudo steady-state (PSS). The results from kinetic measurements at 453−483 K indicate the second H-abstraction step of MCH or MCHE should be kinetically relevant for MCH conversion to MCHE and MCHE conversion to TOL, respectively. At higher temperatures (513−553 K), the kinetically relevant step shifts to the first H-abstraction step of MCH or MCHE for MCH conversion to MCHE and MCHE conversion to TOL, respectively. During MCH dehydrogenation, Pd surfaces are densely covered by the less reactive species (denoted as X*), which form TOL much more slowly than other more reactive intermediates but occupy Pd surfaces at investigated reaction conditions, and dehydrogenation events occur at the interstices within adlayers of species X*. The transition state that mediates the kinetically relevant step of MCH dehydrogenation occupies a certain number of contiguous Pd-atoms, which shows a consistent ratio (∼0.6) to those occupied by the most abundant surface intermediate (MASI).

The proposed mechanism is independent of the mean diameter of Pd nanoparticles and the identity of the support. MCH dehydrogenation rates on Pd nanoparticles show an absence of particle size effects on Al_2O_3 and SiO_2 supports, but vary by a factor of 4 at 453 K and 24 at 393 K as a consequence of the accumulation of X* species. The absence of a particle size effect on MCH dehydrogenation rates is attributed to the dense adlayer of species X* on Pd nanoparticles, which erases the most significant structural differences among differently sized nanoparticles. The support effect, without the requirement of atomic contact between Pd nanoparticles and supports, reflects a difference in accessible Pd-atom ensembles at steady-state at certain reaction conditions. Supports affect the coverages of the less reactive species X* on Pd surfaces in that the Lewis acid−base sites on the supports can scavenge the gaseous counterparts of the less reactive species X* and release more available Pd-atom ensembles for dehydrogenation events. Support effects can only be observed when the less reactive species desorb from metal surfaces reversibly and get scavenged on supports at a significant rate. Overall, the findings here provide detailed mechanistic insights into MCH dehydrogenation on Pd nanoparticles, elucidate the rate enhancements induced by supports for dehydrogenation catalysis, and facilitate catalyst design for H_2 storage and release through liquid organic carriers.

■ ASSOCIATED CONTENT

Supporting Information

The Supporting Information is available free of charge at https://pubs.acs.org/doi/10.1021/acscatal.4c07240.

Characterization of Pd catalysts (TEM and hydrogen chemisorption), standard deactivation correction procedures, kinetic data that are not shown in the main content, and detailed derivation of the kinetic model (PDF)

■ AUTHOR INFORMATION

Corresponding Author

Enrique Iglesia − *University of California, Berkeley, Berkeley, California 94720, United States; Purdue University, West Lafayette, Indiana 47907, United States;* orcid.org/0000-0003-4109-1001; Phone: (925) 323-5559; Email: iglesia@.berkeley.edu, iglesia@purdue.edu

Authors

Zhongyao Zhang − *University of California, Berkeley, Berkeley, California 94720, United States; Shenzhen University, Shenzhen, Guangdong 518005, China;* orcid.org/0000-0001-8537-6821

Sai Chen − *University of California, Berkeley, Berkeley, California 94720, United States; Key Laboratory for Green Chemical Technology of Ministry of Education, School of Chemical Engineering & Technology, Tianjin University, Tianjin 300072, China*

Trenton Otto − *Chevron Technical Center, Richmond, California 94804, United States*

Complete contact information is available at: https://pubs.acs.org/10.1021/acscatal.4c07240

Notes

The authors declare no competing financial interest.

■ ACKNOWLEDGMENTS

The authors acknowledge financial support from the Chevron Corporation and Dr. Andrew Hwang, Dr. Wenshuo Hu, Dr. Nicholas R. Jaegers, and Dr. Ari Fischer for helpful discussions. The authors acknowledge Dr. Gregory Tate for maintaining the H_2 chemisorption equipment.

■ REFERENCES

(1) Bourane, A.; Elanany, M.; Pham, T. V.; Katikaneni, S. P. An overview of organic liquid phase hydrogen carriers. *Int. J. Hydrogen Energy* **2016**, *41* (48), 23075−23091.

(2) Yue, M.; Lambert, H.; Pahon, E.; Roche, R.; Jemei, S.; Hissel, D. Hydrogen energy systems: A critical review of technologies, applications, trends and challenges. *Renewable Sustainable Energy Rev.* **2021**, *146*, No. 111180.

(3) Abe, J. O.; Popoola, A. P. I.; Ajenifuja, E.; Popoola, O. M. Hydrogen energy, economy and storage: Review and recommendation. *Int. J. Hydrogen Energy* **2019**, *44* (29), 15072−15086.

(4) Preuster, P.; Papp, C.; Wasserscheid, P. Liquid Organic Hydrogen Carriers (LOHCs): Toward a Hydrogen-free Hydrogen Economy. *Acc. Chem. Res.* **2017**, *50* (1), 74−85.

(5) Hodoshima, S.; Nagata, H.; Saito, Y. Efficient hydrogen supply from tetralin with superheated liquid-film-type catalysis for operating fuel cells. *Appl. Catal., A* **2005**, *292*, 90−96.

(6) Rahimpour, M. R.; Mirvakili, A.; Paymooni, K. Hydrogen as an energy carrier: A comparative study between decalin and cyclohexane in thermally coupled membrane reactors in gas-to-liquid technology. *Int. J. Hydrogen Energy* **2011**, *36* (12), 6970−6984.

(7) Crabtree, R. H. Hydrogen storage in liquid organic heterocycles. *Energy Environ. Sci.* **2008**, *1* (1), 134−138.

(8) Niermann, M.; Timmerberg, S.; Drünert, S.; Kaltschmitt, M. Liquid Organic Hydrogen Carriers and alternatives for international transport of renewable hydrogen. *Renewable Sustainable Energy Rev.* **2021**, *135*, No. 110171.

(9) Ouma, C. N. M.; Obodo, K. O.; Modisha, P. M.; Bessarabov, D. Si, P, S and Se surface additives as catalytic activity boosters for dehydrogenation of methylcyclohexane to toluene - A liquid organic hydrogen carrier system: Density functional theory insights. *Mater. Chem. Phys.* **2022**, *279*, No. 125728.
(10) Cao, T.; Lee, W.; Huang, R.; Gorte, R. J.; Vohs, J. M. Liquid-Organic hydrogen carriers as endothermic fuels. *Fuel* **2022**, *313*, No. 123063.
(11) Wang, Y.; Shah, N.; Huffman, G. P. Pure Hydrogen Production by Partial Dehydrogenation of Cyclohexane and Methylcyclohexane over Nanotube-Supported Pt and Pd Catalysts. *Energy Fuels* **2004**, *18* (5), 1429−1433.
(12) Horikoshi, S.; Kamata, M.; Sumi, T.; Serpone, N. Selective heating of Pd/AC catalyst in heterogeneous systems for the microwave-assisted continuous hydrogen evolution from organic hydrides: Temperature distribution in the fixed-bed reactor. *Int. J. Hydrogen Energy* **2016**, *41* (28), 12029−12037.
(13) Wijayanta, A. T.; Oda, T.; Purnomo, C. W.; Kashiwagi, T.; Aziz, M. Liquid hydrogen, methylcyclohexane, and ammonia as potential hydrogen storage: Comparison review. *Int. J. Hydrogen Energy* **2019**, *44* (29), 15026−15044.
(14) Alhumaidan, F.; Cresswell, D.; Garforth, A. Hydrogen Storage in Liquid Organic Hydride: Producing Hydrogen Catalytically from Methylcyclohexane. *Energy Fuels* **2011**, *25* (10), 4217−4234.
(15) Obara, S. Energy and exergy flows of a hydrogen supply chain with truck transportation of ammonia or methyl cyclohexane. *Energy* **2019**, *174*, 848−860.
(16) Minachev, K. M.; Caranin, V. I. Dehydrogenation of cyclohexane and hydrogenation of benzene in a fluidized bed of a palladium-alumina catalyst. *Bull. Acad. Sci. USSR, Div. Chem. Sci.* **1963**, *12* (3), 473−475.
(17) Aramendía, M. A.; Borau, V.; Jiménez, C.; Marinas, J. M.; Moreno, A.; Urbano, F. J. Dehydrogenation of cyclohexane over supported Pd catalysts, II. Influence of the support and reduction temperature. *React. Kinet. Catal. Lett.* **1995**, *56* (1), 87−96.
(18) Tien, P. D.; Satoh, T.; Miura, M.; Nomura, M. Continuous hydrogen evolution from cyclohexanes over platinum catalysts supported on activated carbon fibers. *Fuel Process. Technol.* **2008**, *89* (4), 415−418.
(19) Sinfelt, J. H.; Hurwitz, H.; Shulman, R. Kinetics of methylcyclohexane dehydrogenation over Pt-Al_2O_3. *J. Phys. Chem. A* **1960**, *64* (10), 1559−1562.
(20) Usman, M.; Cresswell, D.; Garforth, A. Detailed reaction kinetics for the dehydrogenation of methylcyclohexane over Pt catalyst. *Ind. Eng. Chem. Res.* **2012**, *51* (1), 158−170.
(21) Al-ShaikhAli, A. H.; Jedidi, A.; Anjum, D. H.; Cavallo, L.; Takanabe, K. Kinetics on NiZn Bimetallic Catalysts for Hydrogen Evolution via Selective Dehydrogenation of Methylcyclohexane to Toluene. *ACS Catal.* **2017**, *7* (3), 1592−1600.
(22) Maatman, R.; Ribbens, W.; Vonk, B. The role of Pd-alumina catalyst in the dehydrogenation of cyclohexane. *J. Catal.* **1973**, *31* (3), 384−388.
(23) Li, X.; Shen, P.; Han, X.; Wang, Y.; Zhu, Y.; Wu, Z. Dehydrogenation mechanisms of liquid organic hydrogen carriers over Pt, Pd, Rh, and Ni surfaces: Cyclohexane as a model compound. *Appl. Surf. Sci.* **2021**, *543*, No. 148769.
(24) Coq, B.; Dutartre, R.; Figueras, F.; Tazi, T. Particle size, precursor, and support effects in the hydrogenolysis of alkanes over supported rhodium catalysts. *J. Catal.* **1990**, *122* (2), 438−447.
(25) Ding, X.; Zhu, H.; Ren, H.; Liu, D.; Yu, Z.; Shi, N.; Guo, W. Adsorption and dehydrogenation of C_2−C_6 n-alkanes over a Pt catalyst: a theoretical study on the size effects of alkane molecules and Pt substrates. *Phys. Chem. Chem. Phys.* **2020**, *22* (38), 21835−21843.
(26) Wang, J.; Liu, H.; Fan, S.; Li, W.; Li, Z.; Yun, H.; Xu, X.; Guo, A.; Wang, Z. Size-Dependent Catalytic Cyclohexane Dehydrogenation with Platinum Nanoparticles on Nitrogen-Doped Carbon. *Energy Fuels* **2020**, *34* (12), 16542−16551.
(27) Corma, A.; Martin, M. A.; Pajares, J. A.; Perez-Pariente, J.; Avalos, M.; Yacaman, M. J. Determination of the specific activity for methylcyclohexane dehydrogenation of different surface orientations of palladium-supported catalysts. *J. Mol. Catal.* **1988**, *48* (2), 199−205.
(28) Ramos, A. L. D.; da Silva Alves, P.; Aranda, D. A.; Schmal, M. Characterization of carbon supported palladium catalysts: inference of electronic and particle size effects using reaction probes. *Appl. Catal., A* **2004**, *277* (1−2), 71−81.
(29) Passos, F. B.; Aranda, D. A.; Schmal, M. Characterization and Catalytic Activity of Bimetallic Pt-In/Al_2O_3 and Pt-Sn/Al_2O_3 Catalysts. *J. Catal.* **1998**, *178* (2), 478−488.
(30) Allian, A. D.; Takanabe, K.; Fujdala, K. L.; Hao, X.; Truex, T. J.; Cai, J.; Buda, C.; Neurock, M.; Iglesia, E. Chemisorption of CO and Mechanism of CO Oxidation on Supported Platinum Nanoclusters. *J. Am. Chem. Soc.* **2011**, *133* (12), 4498−4517.
(31) Iglesia, E. Design, synthesis, and use of cobalt-based Fischer−Tropsch synthesis catalysts. *Appl. Catal., A* **1997**, *161* (1−2), 59−78.
(32) Flaherty, D. W.; Iglesia, E. Transition-State Enthalpy and Entropy Effects on Reactivity and Selectivity in Hydrogenolysis of n-Alkanes. *J. Am. Chem. Soc.* **2013**, *135* (49), 18586−18599.
(33) Flaherty, D. W.; Hibbitts, D. D.; Iglesia, E. Metal-Catalyzed C−C Bond Cleavage in Alkanes: Effects of Methyl Substitution on Transition-State Structures and Stability. *J. Am. Chem. Soc.* **2014**, *136* (27), 9664−9676.
(34) García-Diéguez, M.; Hibbitts, D. D.; Iglesia, E. Hydrogen Chemisorption Isotherms on Platinum Particles at Catalytic Temperatures: Langmuir and Two-Dimensional Gas Models Revisited. *J. Phys. Chem. C* **2019**, *123* (13), 8447−8462.
(35) Fischer, A. F.; Iglesia, E. The nature of "hydrogen spillover": Site proximity effects and gaseous intermediates in hydrogenation reactions mediated by inhibitor-scavenging mechanisms. *J. Catal.* **2023**, *420*, 68−88.
(36) Jiang, N.; Rao, K. R.; Jin, M.-J.; Park, S.-E. Effect of hydrogen spillover in decalin dehydrogenation over supported Pt catalysts. *Appl. Catal., A* **2012**, *425*−*426*, 62−67.
(37) Gao, Z.; Wang, G.; Lei, T.; Lv, Z.; Xiong, M.; Wang, L.; Xing, S.; Ma, J.; Jiang, Z.; Qin, Y. Enhanced hydrogen generation by reverse spillover effects over bicomponent catalysts. *Nat. Commun.* **2022**, *13* (1), No. 118.
(38) Benson, J. E.; Kohn, H. W.; Boudart, M. On the reduction of tungsten trioxide accelerated by platinum and water. *J. Catal.* **1966**, *5* (2), 307−313.
(39) Levy, R. B.; Boudart, M. The kinetics and mechanism of spillover. *J. Catal.* **1974**, *32* (2), 304−314.
(40) Prins, R. Hydrogen Spillover. Facts and Fiction. *Chem. Rev.* **2012**, *112* (5), 2714−2738.
(41) Chin, Y.-H.; García-Diéguez, M.; Iglesia, E. Dynamics and Thermodynamics of Pd−PdO Phase Transitions: Effects of Pd Cluster Size and Kinetic Implications for Catalytic Methane Combustion. *J. Phys. Chem. C* **2016**, *120* (3), 1446−1460.
(42) Chin, Y.-H.; Buda, C.; Neurock, M.; Iglesia, E. Consequences of Metal−Oxide Interconversion for C−H Bond Activation during CH_4 Reactions on Pd Catalysts. *J. Am. Chem. Soc.* **2013**, *135* (41), 15425−15442.
(43) Nitta, T. S.; Shigetomi, T.; Kuro-Oka, M.; Katayama, T. An adsorption isotherm of multi-site occupancy model for homogeneous surface. *J. Chem. Eng. Jpn.* **1984**, *17* (1), 39−45.
(44) Bergeret, G.; Gallezot, P.Particle Size and Dispersion Measurements. In *Handbook of Heterogeneous Catalysis*; John Wiley & Sons, 2008; p 439.
(45) Kroenlein, K. G.; Muzny, C. D.; Kazakov, A. F.; Diky, V.; Chirico, R. D.; Magee, J. W.; Abdulagatov, I. M.; Frenkel, M. D. NIST/TRC Web Thermo Tables (WTT) NIST Standard Reference Subscription Database 3-Professional Edition Version 2, 2011. http://wtt-pro.nist.gov/. (Accessed September 11, 2024).
(46) Tang, M.; Larish, W. A.; Fang, Y.; Gankanda, A.; Grassian, V. H. Heterogeneous Reactions of Acetic Acid with Oxide Surfaces: Effects of Mineralogy and Relative Humidity. *J. Phys. Chem. A* **2016**, *120* (28), 5609−5616.

https://doi.org/10.1021/acscatal.4c07240
ACS Catal. 2025, 15, 676−696

(47) Hasan, M. A.; Zaki, M. I.; Pasupulety, L. Oxide-catalyzed conversion of acetic acid into acetone: an FTIR spectroscopic investigation. *Appl. Catal., A* **2003**, *243* (1), 81−92.
(48) Wang, S.; Iglesia, E. Experimental and theoretical assessment of the mechanism and site requirements for ketonization of carboxylic acids on oxides. *J. Catal.* **2017**, *345*, 183−206.
(49) Wang, S.; Iglesia, E. Experimental and Theoretical Evidence for the Reactivity of Bound Intermediates in Ketonization of Carboxylic Acids and Consequences of Acid−Base Properties of Oxide Catalysts. *J. Phys. Chem. C* **2017**, *121* (33), 18030−18046.
(50) Peereboom, M.; van de Graaf, B.; Baas, J. M. A. Experimental and calculated thermodynamic data for the isomeric methylcyclohexenes and methylenecyclohexane. *Recl. Trav. Chim. Pays-Bas* **1982**, *101* (10), 336−338.
(51) Martín, A. J.; Mitchell, S.; Mondelli, C.; Jaydev, S.; Pérez-Ramírez, J. Unifying views on catalyst deactivation. *Nat. Catal.* **2022**, *5* (10), 854−866.
(52) Burwell, R. L. The surface organometallic zoo-continued. *Catal. Lett.* **1990**, *5* (3), 237−255.
(53) Anslyn, E. *Modern Physical Organic Chemistry*; University Science Books, 2006.

https://doi.org/10.1021/acscatal.4c07240
ACS Catal. 2025, 15, 676−696